GENERALIZED MODEL AND APPLICATIONS FOR VOLATILE MEMRISTIVE DEVICES

A Thesis
Presented to
The Academic Faculty

by

Joshua C. Shank

In Partial Fulfillment
of the Requirements for the Degree
Master's of Science in the
School of Electrical and Computer Engineering

Georgia Institute of Technology
August 2015

GENERALIZED MODEL AND APPLICATIONS FOR VOLATILE MEMRISTIVE DEVICES

Approved by:

Dr. William Alan Doolittle, Advisor
School of Electrical and Computer Engineering
Georgia Institute of Technology

Dr. Paul Douglas Yoder
School of Electrical and Computer Engineering
Georgia Institute of Technology

Dr. Faisal Alamgir
School of Materials Science and Engineering
Georgia Institute of Technology

Date Approved: 7/23/2015

ACKNOWLEDGEMENTS

I wish to thank my parents for teaching and supporting me throughout these many years. I would also like to thank my teachers and particularly my advisor Dr. Alan Doolittle for many helpful conversations and brainstorming sessions that led to this work. This work would not have been possible without the other members of the Advanced Semiconductor Research Facility, specifically Jordan Greenlee, Brooks Tellekamp, Brendan Gunning, and Chloe Fabien.

TABLE OF CONTENTS

LIST OF TABLES

LIST OF FIGURES

SUMMARY

As the performance of digital computing saturates due to material and size limitations, new computing paradigms are being investigated. Chapter 1 will introduce neuromorphic computing as one of these computing paradigms. Within the field of neuromorphic computing, the role of memristive devices has become increasingly important since the first reported physical memristor in 2008. Chapter 2 discusses a brief history of memristors, their role in modern neuromorphic computing, and how these devices have been modelled for use in large scale circuit simulations.

Among the many types of memristors discussed in Chapter 2, mixed ion-electron memristors have shown particular promise for neuromorphic computing. Chapter 3 explores the physical mechanism of activated ion hopping conductivity within these devices and concludes with a simple generalized set of equations to describe these devices.

Chapter 4 provides two examples for the model derived in Chapter 3. The first example is the well-studied nanoscale non-volatile memristor based in the TiO_2 system, while the second example is a macroscopic volatile memristor based in the $LiNbO_2$ material system. Both examples are compared to experimental results and several previously unexplained phenomenon are discussed using results from the physics based model.

The application of volatile memristive devices is explored in Chapter 5 by examining the effect of these devices on an example neuromorphic sub-circuit. It is shown that the addition of a volatile memristor to the voltage divider in a Schmitt Trigger circuit can implement spike-frequency adaption without increasing the circuit

complexity. Such volatile dynamics have been shown to control signal propagation, improve signal-to-noise ratio, and control debilitating instabilities such as seizures in biological neurons.

CHAPTER 1

INTRODUCTION

1.1 *Motivation*

Modern computing based on silicon CMOS technology is approaching performance limits driven by fundamental physical limits, material limits, and device limits. The 2013 ITRS roadmap shows saturating feature sizes and the end of Moore's Law within 10 – 20 years [1]. While engineering challenges, such as diffraction limits, that were predicted to end Moore's Law have been overcome by novel engineering solutions, such as computational lithography [2], the new limits are driven by fundamental physical phenomenon. With the release of the 22 nm node in 2012, parasitic resistances begin to dominate the transistor performance [3]. The 14 nm node released in 2014 with gate lengths near 5 nm has begun to reach limitations where direct drain to source tunneling limits performance [4, 5]. These limitations can be seen in the saturation of clock speed, power, and single thread performance shown in Figure 1 [6].

While general purpose CMOS computers are beginning to encounter scaling and performance limits, application specific technologies have already been implemented to improve tasks such as biomolecular simulations and video decoding [2]. Diversifying the computing paradigm may add new functionality to specific applications through emerging technologies such as quantum computing, spintronics, optical computing, or neuromorphic computing.

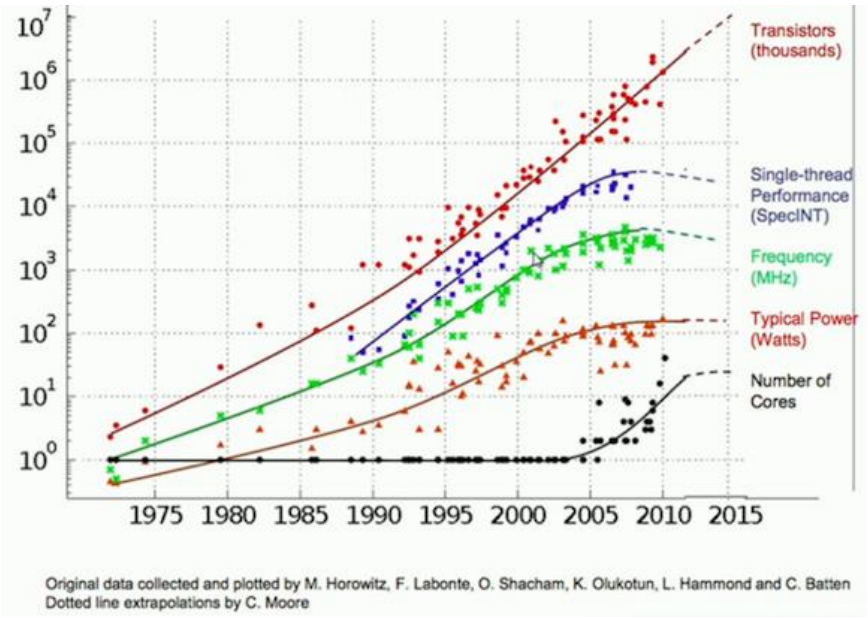

Figure 1: Comparison of general purpose CMOS chip performance since the 1970's and the saturation in power, frequency, and performance despite increasing transistor counts.

1.2 *Background*

Neuromorphic computing is computation performed on analog or mixed analog/digital circuits designed to mimic the computation performed in biological nervous systems [7]. Characteristics of computation in biological systems are extremely low power consumption and massively parallel computation. While biological systems perform poorly at tasks such as basic arithmetic, they excel at pattern recognition, control, and processing of noisy or incomplete information. By replicating the architecture of biological systems, neuromorphic computing is expected to also excel in these applications.

Early neuromorphic circuits replicated the differential equation models of a neuron using analog circuits based on established microfabrication technologies [8, 9]. Since the introduction of nanoscale non-volatile filamentary memristors in 2008 and their

behavioral similarities to biological processes [10], neuromorphic circuits have increasingly incorporated memristor technologies [11-15]. Despite the inclusion of memristors in neuromorphic circuitry, little attention has been given to the volatile dynamics of the mammalian brain and the corresponding importance of volatile memristors. These volatile dynamics have been shown to control signal propagation [16], improve signal-to-noise ratio [17], and inhibit debilitating instabilities such as seizures [18].

1.3 *Organization of Thesis*

In Chapter 2, the history of memristors and their application to neuromorphic computing is introduced. Because memristors fundamentally require the modulation of a storable property that affects resistance, there are many different types of memristors. Chapter 2 includes an overview of a few select memristor classes divided based on the property being changed. Of the many memristor classes, mixed ion-electron memristors have been particularly successful in neuromorphic computing perhaps because of the physical similarities to ion conduction in biological systems. Chapter 2 concludes with a review of previous modelling work in mixed ion-electron memristors enabling large scale circuit simulations and the limitations of those models.

The basis of this work is a mixed ion-electron memristor model derived in Chapter 3. This model is based on activated hopping conduction of mobile ions within a memristive material. While this physical basis could be applied to complex device models such as finite element models, such models are too computationally intensive for large scale circuit simulations. Therefore, a characteristic equation model for mixed ion-

electron memrsitors is derived from the activated hopping conductivity framework and the frequency dependent behavior of this model is explored in Chapter 3.

Chapter 4 provides two specific device examples of the characteristic equation model to demonstrate the extremes encountered in mixed ion-electron memristors. The first example device is a nanoscale memristor based in the TiO_2 material system. These devices were the first reported memristors, developed by HP labs in 2008 [10]. As such, they have received considerable attention, are well documented, and provide a valuable verification standard for new models. The second example is a macroscopic memristor based in the $LiNbO_2$ material system with a low activation energy for ion motion. This results in volatile behavior.

Having developed the history of memristors in Chapter 2, the physical framework for modeling memristors in Chapter 3, and device models in Chapter 4, an example circuit application for volatile memristors is developed in Chapter 5. The goal of such circuits is to implement biologically realistic volatile behavior in a circuit relevant to neuromorphic computing without significantly increasing the circuit complexity. The circuit examined is a Schmitt Trigger circuit, which is useful for threshold detection and neural spike generation. It is shown that inclusion of a volatile memristor in this circuit creates an implementation for spike frequency adaptation, which is important for neural stability in biological systems [18].

The thesis concludes with Chapter 6 and a discussion of future work, particularly theoretical and modelling options.

CHAPTER 2

MEMRISTORS

2.1 *History and Background*

The memristor was first proposed as the fourth fundamental two-terminal passive circuit element by Leon Chua in 1971 [19]. The primary argument for the inclusion of the memristor was a matter of symmetry. There are four fundamental quantities when considering the passive circuit elements: charge (q), current (I), voltage (V), and flux-linkage (ϕ). These four quantities can be related to each other in six ways, shown in Equations 2.1a-f. The relations between charge to current and voltage to flux-linkage are fundamental definitions. Three of the remaining four relations describe the well-known passive devices: a resistor (voltage to current), a capacitor (charge to voltage), and an inductor (flux-linkage to current). Chua's 1971 paper theorized a fourth device that would relate flux-linkage and charge. A theoretical development of this relationship revealed that the device would act like a variable resistor with memory of its input. Thus the name memristor was given [19].

Fundamental Definition	$dq = I * dt$	Equation 2.1a
Fundamental Definition	$d\phi = V * dt$	Equation 2.1b
Resistor	$dV = R * dI$	Equation 2.1c
Capacitor	$dq = C * dV$	Equation 2.1d
Inductor	$d\phi = L * dI$	Equation 2.1e
Memristor	$d\phi = M * dq$	Equation 2.1f

In 1976, Chua expanded the memristor definition to include a class of devices termed memristive systems [20]. These devices are described by a set of dynamic relations, shown in Equations 2.2a-b, that include the original memristor definition but

allow for more complex behavior such as multiple inputs, $\vec{u}$, multiple outputs, $\vec{y}$, and multiple internal mechanisms described by the state variables, $\vec{x}$, allowing for threshold voltages and volatile behavior.

$$\vec{y} = g(\vec{x}, \vec{u}, t) * \vec{u} \qquad \text{Equation 2.2a}$$

$$\frac{d\vec{x}}{dt} = f(\vec{x}, \vec{u}, t) \qquad \text{Equation 2.2b}$$

These additional behaviors are important for physical devices because no physical implementation of a memristor has been shown to follow the more restrictive 1971 definition. The major classes of memristive devices are reviewed in Section 2.3.

2.2 *Memristors in Neuromorphic Computing*

Neuromorphic computing began in the late 1980's with the impending realization of power and speed limitations in traditional CMOS technology [7]. The goal of neuromorphic computing is to replicate the brain's 10^{16} complex operations per second while only using a few watts of power. This was originally attempted by reproducing the mathematical models of a neuron using analog VLSI technology [21, 22].

Fundamentally, the neural computation architecture is a massively parallel system of neurons operating at low frequency with integrated computation and memory. The human brain has approximately 100 billion neurons each of which is communicating with 1000 – 10,000 synaptic connections [23]. Instead of switching between digital values, the brain performs computation by the generation, scaling, and integration of voltage spikes called action potentials. Each of these functions exists as an analog variable with changes in the spike rate, spike amplitude, and spike shape. There are a variety of theories for how the brain encodes information in these spikes and evidence that multiple methods may be applied in the brain [24]. Memory in biological systems is also an active area research,

although at least one form of memory is stored in the dynamic scaling of synaptic inputs [25].

Although the mechanisms of computation in biological systems are still active areas of research, a general model exists for replicating the neural architecture in a neuromorphic chip. The input to each neuron is a collection of 1000 to 10,000 synapses. Each synapse receives a voltage spike from the presynaptic neuron and generates a scaled current into the post synaptic neuron. The input currents are summed through the dendritic tree and integrated on the neuron's cell body. The cell body typically sits at a non-zero resting potential dictated by the distribution of ions inside and outside the cell. The input current charges the cell body to a potential above the resting potential. Once the cell voltage exceeds a threshold, voltage gated channels allow potassium and sodium ions to flow through the cell wall. These ion currents create a voltage spike that is then propagated to the next set of neurons [25]. The steps of this process are shown in Figure 2.

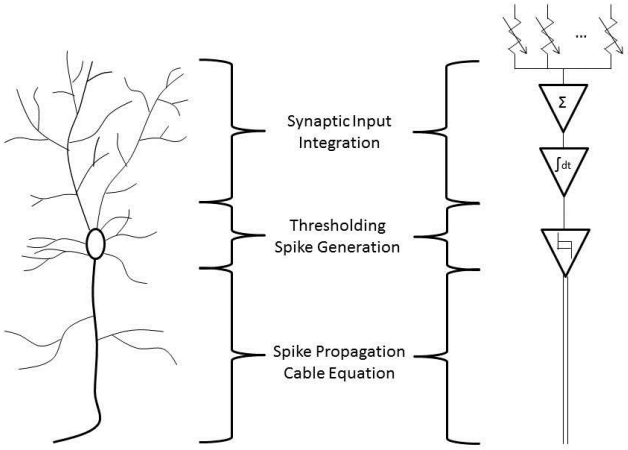

Figure 2: The general steps of a biological neuron replicated in analog circuitry are: synaptic input, integration, thresholding, spike generation, and spike propagation.

While memristors were first theorized in 1971 [19], it was the 1976 paper on memristive systems that first introduced the connection between memristive systems and neural processes [20]. It was shown that the potassium and sodium ion channels in a neuron, modelled by the Hodgkin-Huxley model [26], could be represented by memristive systems. The connection between memristive systems and neurobiology was again examined with the first reported physical memristor in 2008 by HP labs [10]. Since then memristors have been incorporated into neuromorphic circuits to implement synaptic functionality [11, 13-15], spike generation [11, 12], and spike propagation [27].

Memristors are valuable for implementing synaptic functionality because they are a resistive element capable of scaling an input voltage into a current and they contain memory of previous inputs. One memory mechanism implemented in memristors [15] and experimentally observed in biological neurons [28] is spike timing dependent plasticity. The use of memristors for spike generation has been demonstrated, but is generally less useful because they require well-conditioned inputs to take advantage of the memristor's frequency dependent behavior [12] and spike generation can be accomplished simply with CMOS technology [11].

2.3 *Major Categories of Memristors*

While memristors were first theorized in 1971 and first experimentally reported in 2008, a review of historical devices reveals memristive behavior in a wide range of devices including tungsten filament lamps, vapor discharge tubes, and thermistors [29]. The following sub-sections summarize a few of the major classes of memristors that have received attention since the 2008 publication reintroduced memristors to the research

community. Other memristor summaries have been tabulated elsewhere including comparisons of switching speed, retention time, and endurance [30].

2.3.1 Filamentary Memristors

The filamentary memristor was first published by HP labs in 2008 [10], although filamentary resistive switching devices were published and well characterized before this [31]. Fundamentally these devices operate by the creation and destruction of a conducting filament through an otherwise insulating material. When the filament connects the electrodes together a low resistance state exists and when the filament is broken a high resistance state exists. The formation of the filament requires the motion of mobile ions such as oxygen anions in TiO_2 [10], NiO [32], WO_x [33], TaO_x [34], or NbO_x [35], or metal cations in Ag_2S or GeSe [31]. While these devices are typically binary, careful control of timing and compliance currents can program analog resistance states by controlling the distance between the filament edge and one electrode [36].

Filamentary memristors can be further divided into unipolar and bipolar devices. Unipolar devices are capable of switching when a voltage of either polarity is applied. Filament formation occurs at a fairly low voltage while filament destruction occurs at a higher voltage. These devices are often compared to a nano-scale fuse [31]. In contrast, bipolar filamentary memristors require voltages of opposite polarities to switch between the high and low resistance states by electrically drifting the mobile ions in each direction.

Filamentary memristors are typically not manufactured with the filaments preformed and filaments must by initialized by an electroforming process. This process requires higher voltage and current than normal operation and has been shown to cause

electrode damage in switchable oxides as mobile oxygen bursts through the electrode [37, 38]. In addition to the filament formation, filamentary memristor operation creates extreme thermal and electrical conditions. It is estimated that a switching memristor produces power densities on the order of 10^{12} W/cm^3 [31] reaching temperatures of 800 K [39] and electric fields above 10^6 V/cm [40].

2.3.2 Mobile Ion Wavefront Memristors

While filamentary memristors can be considered one geometry of mixed ion-electron conducting (MIEC) memristors, another geometry is the mobile ion wave front memristor. This geometry is similar to the bipolar switching filamentary memristor, but no filament is formed. Instead, mobile dopants move throughout a host lattice creating regions of highly doped and semi-insulating material.

One example of this geometry is the cosputtered Ag/Si memristor in which the conduction front is created by introducing the dopant silver part of the way into a silicon deposition. This eliminates the need for electroforming as the device is fully formed during fabrication [41]. Mobile ion wave front devices have demonstrated nearly analog switching, but have not been demonstrated with as wide a dynamic range (R_{ON} / R_{OFF}) as filamentary memristors.

Another example of mobile ion wave front memristors is the volatile memristor $LiNbO_2$. This material grown by molecular beam epitaxy [42] or liquid phase electro-epitaxy [43] is deposited with uniform composition. Electrical modulation of the lithium ion dopants produces a memristive response that relaxes back to an equilibrium state when the input is removed.

2.3.3 Oxidation/Reduction Memristors

While memristors were originally defined as two terminal devices [19], the memristive system definition allows for multiport systems [20]. Such memristive systems have been demonstrated in mobile ion systems in which the mobile ions are allowed to leave the memristive material through a gated electrolyte. This three terminal transistor structure results in the oxidation or reduction of the active material changing the conductance between the source and drain terminals. Experimental examples of this structure include the oxidation/reduction of organic materials [44] and the lithiation of inorganic battery cathodes [45]. These three terminal devices are important for neuromorphic applications because many biological models include batteries with variable resistance [26] and the biological synapse is fundamentally a three terminal device – involving the presynaptic neuron, the post-synaptic neuron, and the intracellular fluid – although it is often replaced by two terminal memristors in neuromorphic circuits.

2.3.4 Spintronic Memristors

While mobile ion-electron conducting memristors modify the electron conductivity either with doping or phase transitions, memristive effects have also been observed in materials where resistance modulation and memory are provided by a degree of freedom other than mobile ions. One such system is the broad class of spintronic devices where electron transport is sensitive to the electron-spin polarization, which can be changed by an externally applied voltage [46]. By controlling the ferromagnetic polarization of a free polarization layer compared to a reference polarization layer across a tunneling junction, the current flow through the tunnel junction can be controlled [47]. Many of these devices can also be switched by an external magnetic field [48] making them multi-input devices best described by the memristive system formalism.

2.3.5 Ferroelectric Switches

Similar to the spintronic memristors are ferroelectric memristors where device resistance is controlled by the ferroelectric polarization near a tunnel barrier. For nanoscale devices with small domains, a nearly continuous range of resistances can be achieved [49].

2.3.6 Mott Metal-Insulator Switches

In addition to ion motion, magnetic polarization, and electric polarization, thermal energy can provide a degree of freedom capable of producing memristive behavior. In materials with a Mott metal-insulator transition, joule heating has been demonstrated to produce memristive effects. When sufficient voltage is applied to heat the device above the metal-insulator transition temperature, the device switches to a conducting state. The conducting state (higher current) dissipates more power, requiring a lower voltage to switch back to the insulating state [27].

2.4 *Memristor Models*

In an effort to understand memristive switching and its effects in potential applications, many models have been produced. These models can generally be divided into two categories: physical models and characteristic equation models. Physical models attempt to explain the fundamental mechanisms involved in memristive switching. These models vary in complexity from sets of dynamic equations describing physical phenomenon [50, 51] to full finite element models [39, 52]. Most of the physical models published have focused on the mobile ion memristors and explored a variety of physical phenomenon including: ion drift [10], electrochemical potential [50], ionic boundary

conditions [53], multiple parallel filaments [54], joule heating [39], thermal gradients [51], and structural geometry [39, 52].

In contrast, characteristic equation models attempt to produce computationally inexpensive descriptions of memristor operation for applications in circuit modelling software. These models tend to be based in the memristor formalisms developed by Chua [19, 20] and are informed to varying degrees by the physics of the modelled device [27, 53, 55]. The model developed herein is a generalized characteristic equation model informed by the physics of activated ionic hopping conductivity. It will be shown that this model is applicable to a wide range of mobile ion memristors and reproduces effects that have been experimentally observed and modelled by more complex simulations.

CHAPTER 3

MEMRISTOR MODEL DERIVATION

3.1 *Activated Mobile Ion Hopping Conduction*

Ion conduction between discretely bound sites can be described by hopping conductivity where the hopping frequency (Γ) is given by Equation 3.1 [56, 57].

$$\Gamma = \left[\omega_o(1-c)e^{-\left(\frac{2d}{\alpha}\right)}\right]e^{-\left(\frac{E_A}{kT}\right)} \qquad \text{Equation 3.1}$$

Where ω_o is the hopping attempt frequency (related to the phonon frequency), c is the probability of finding an occupied site at the hopping destination and is dependent on the vacancies present, d is the hopping distance, E_A is the energy barrier between hopping sites, k is the Boltzmann constant, T is temperature in Kelvin, and α is a localization parameter related to the extent of the ion's wavefunction. While we retain the full equation as described by Mott [56, 57], this general form of Equation 3.1 is often simplified by replacing the bracketed term with one value by combining the distance dependence into the attempt frequency and ignoring the probability of finding an unoccupied site, which is acceptable for dilute concentrations.

When exposed to an electric field E, the energy barrier E_A is lowered by qEd in the direction of the electric field and raised by the same amount opposing the electric field, as shown in Equation 3.2, where q is the charge of an electron.

$$\Gamma = \omega_o(1-c)e^{-\left(\frac{2d}{\alpha}\right)}e^{-\left(\frac{E_A-qEd}{kT}\right)} \qquad \text{Equation 3.2}$$

The resulting current density, J_{ij}, from site i to neighboring site j with corresponding ion concentration N_i and N_j can be described by Equation 3.3.

$$J_{ij} = ZqdN_i\Gamma_{ij} - ZqdN_j\Gamma_{ji}$$ Equation 3.3

where Z is the charge of the ion. Substituting the hopping frequency into the above equation and separating common terms yields Equation 3.4.

$$J_{ij} = ZqdN_o\omega_o e^{-\left(\frac{2d}{\alpha}\right)}\left[c_i\left(1-c_j\right)e^{-\left(\frac{E_A-qEd}{kT}\right)} - c_j(1-c_i)e^{-\left(\frac{E_A+qEd}{kT}\right)}\right]$$

Equation 3.4

where the concentrations N_i and N_j are separated into the stoichiometric concentration N_o and the probability of finding an ion at that site c_i such that $N_i = N_o c_i$ and likewise for site j. Equation 3.4 can be reduced to Equation 3.5 by separating the common activation energy term.

$$J_{ij} = Zqd\omega_o N_o e^{-\left(\frac{2d}{\alpha}\right)}e^{-\left(\frac{E_A}{kT}\right)}\left[c_i e^{\left(\frac{qEd}{kT}\right)} - c_j e^{-\left(\frac{qEd}{kT}\right)} - 2c_i c_j \sinh\left(\frac{qEd}{kT}\right)\right]$$

Equation 3.5

3.2 *Linearized Model*

Initially, we will linearize Equation 3.5 for small electric fields to define an ion mobility. Later we will modify the mobility to account for the high field non-linear kinetics. The generalized form of hopping conductivity current density, Equation 3.5, can be linearized for small electric fields where the concentration gradient is small and the exponential terms are nearly linear. The bracketed term in Equation 3.5 is shown in Figure 3 as a function of the electric field.

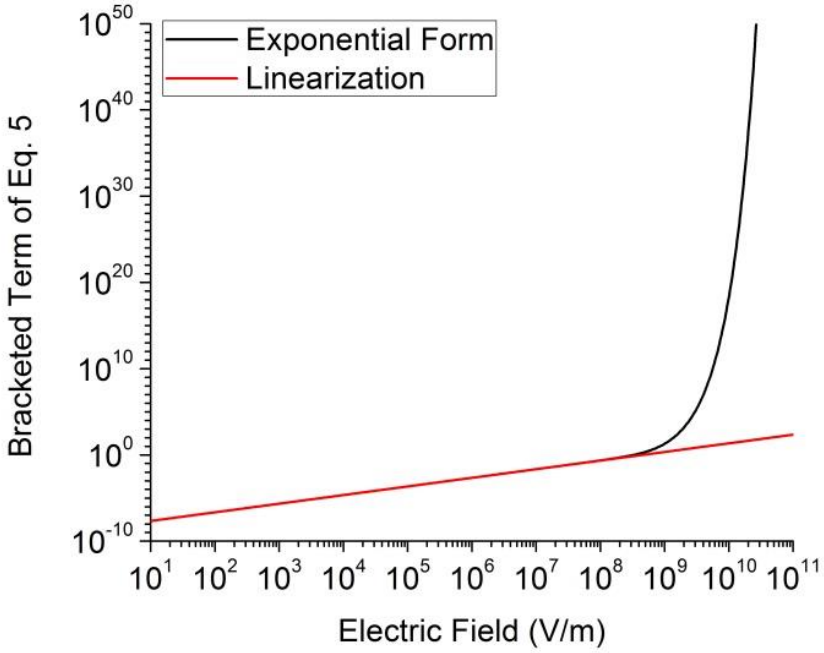

Figure 3: The bracketed terms in the full exponential form of hopping conductivity, Equation 3.5, and the linearized form, Equation 3.8. The linear approximation matches the exponential form at low electric fields but diverges at high electric fields. This data was calculated using d = $3x10^{-10}$ m and T = 800K.

As shown in Figure 3, the linear approximation is not valid for fields as high as 10^{10} V/m, as are experienced during the breakdown of filamentary memristors, but is approximately true for fields as high as 10^{8} V/m, which covers most of the practical breakdown fields in real materials. Therefore, for large devices, such as previously published $LiNbO_2$ memristors [58], with length scales on the order of 100 μm and low electric fields, the ion current can be linearized. However, for filamentary memristors with length scales less than 100 nm, electric fields may locally exceed 10^{8} V/m due to the distribution of dopants and the full exponential form of the ion current should be used.

The linearized form of the electric field modified activation energy is given by Equation 3.6.

$$e^{-\left(\frac{E_A - qdE}{kT}\right)} \approx e^{-\left(\frac{E_A}{kT}\right)}\left(1 + \frac{qdE}{kT}\right) \qquad \text{Equation 3.6}$$

Substituting this linearization into the hopping current density, Equation 3.4, yields the linearized ion current density, Equation 3.7, which can be further simplified into Equation 3.8.

$$J_{ij} = ZqdN_o\omega_o e^{-\left(\frac{2d}{\alpha}\right)}\left[c_i(1-c_j)e^{-\left(\frac{E_A}{kT}\right)}\left(1+\frac{qdE}{kT}\right) - c_j(1-c_i)e^{-\left(\frac{E_A}{kT}\right)}\left(1-\frac{qdE}{kT}\right)\right] \quad \text{Equation 3.7}$$

$$J_{ij} = ZqdN_o\omega_o e^{-\left(\frac{2d}{\alpha}\right)}e^{-\left(\frac{E_A}{kT}\right)}\left[\left(c_i + c_j - 2c_ic_j\right)\left(\frac{qdE}{kT}\right) + \left(c_i - c_j\right)\right] \quad \text{Equation 3.8}$$

By factoring the bracketed term, the linearized ion hopping current equation appears as a classical drift – diffusion equation, shown in Equation 3.9, where the mobility and diffusion coefficient become concentration dependent, as shown in Equations 3.10 – 3.12.

$$J_{ij} = Zqd^2N_o\omega_o e^{\left(\frac{-2d}{\alpha}\right)}e^{-\left(\frac{E_A}{kT}\right)}\left(c_i + c_j - 2c_ic_j\right)\frac{q}{kT}\left[E - \frac{kT}{q}\left(\frac{1}{c_i+c_j-2c_ic_j}\right)\frac{\left(c_j-c_i\right)}{d}\right]$$

$$= ZqN\left(\mu_{hopping}E - D\frac{\left(c_j-c_i\right)}{d}\right) \quad \text{Equation 3.9}$$

Where,

$$\mu_{hopping} = 2\omega_o d^2 e^{\frac{-2d}{\alpha}}e^{-\frac{E_A}{kT}}\left[\frac{kT}{q}\right]^{-1}\left(1-\frac{2c_ic_j}{c_i+c_j}\right) \quad \text{Equation 3.10}$$

$$N = N_o\frac{c_i+c_j}{2} \quad \text{Equation 3.11}$$

$$D = \frac{1}{2}\frac{kT}{q}\left(\frac{c_i+c_j}{\left(c_i+c_j-2c_ic_j\right)^2}\right)\mu_{hopping} \quad \text{Equation 3.12}$$

It is important to note that the linearized current density equation is only valid for modestly high electric fields. However, in order to model ionic systems with extremely large local electric fields, such as a filamentary memristor, an additional factor must be included to account for the nonlinearity.

3.3 *1-Dimentional Mobile Ion Distribution*

Examining the effective local carrier motion probability ($c_i + c_j - 2c_ic_j$) from Equation 3.9, shown in Figure 4, for a smooth distribution of ions ($c_i \approx c_j$), shown as a blue line, the effective local carrier concentration reaches a maximum of 0.5 at a carrier density of half the stoichiometric value and goes to zero as the number of carriers approaches 0% or 100% of the stoichiometric value. As the carrier motion probability goes to zero, the diffusion coefficient goes to infinity. The ability to tune the diffusion coefficient will be important to the stability of adaptive circuits using volatile memristors in Chapter 5.

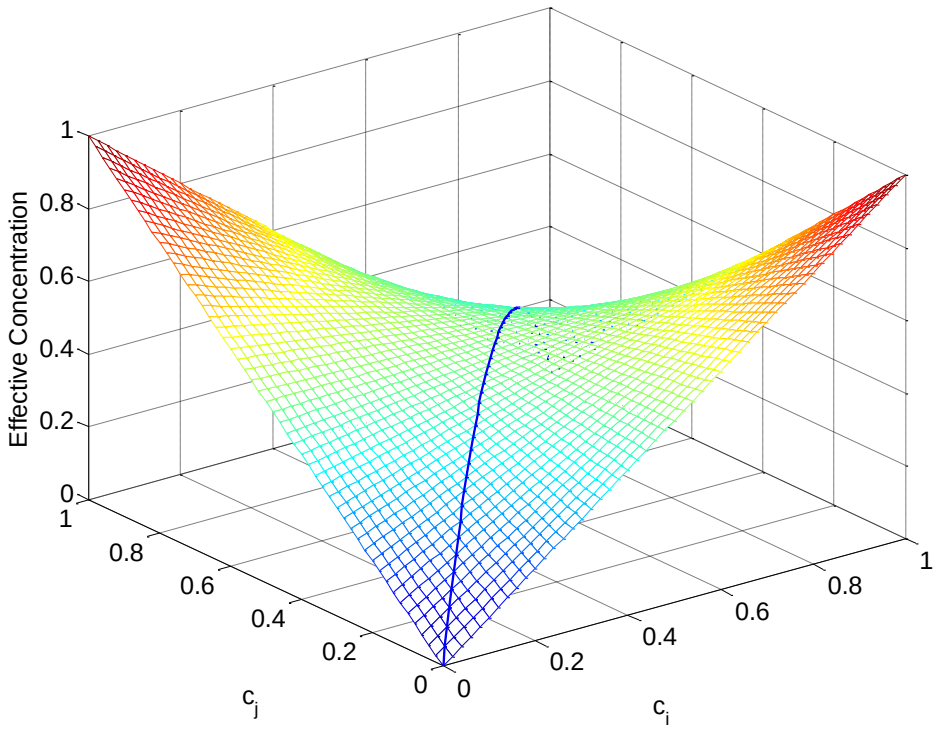

Figure 4: The effective local carrier concentration as a function of the real carrier concentrations at site i and site j.

Examining the ion current density, Equation 3.9, it is possible to solve for the steady state distribution of ions for a given electric field by recognizing that when J = 0 an iterative solution can be given for the mobile ion distribution, shown in Equation 3.13.

$$c_j = \frac{\left(1+\frac{qd}{kT}E\right)c_i}{1-(1-2c_i)\frac{qd}{kT}E} \qquad \text{Equation 3.13}$$

In general, the electric field is not a constant across the length of the device because the mobile ions are also dopants. Accounting for the changing electric field can be accomplished by recognizing that the local electric field is related to the local concentration of dopants via the resistivity as shown in Equation 3.14.

$$E_i = \frac{V}{\Delta x}\frac{\frac{1}{(1-c_i)+c'}}{\sum_0^n \frac{1}{(1-c_i)+c'}} \qquad \text{Equation 3.14}$$

Where c' is the normalized concentration of immobile dopants. Examining the limiting case where all the dopants are mobile (c' = 0), the distribution of ions is shown in Figure 5 for devices of different lengths. The computed distributions are for an average normalized concentration of mobile dopants equal to 0.7, an applied voltage of 1V, and device lengths varying from 10^{-7} m to 10^{-2} m.

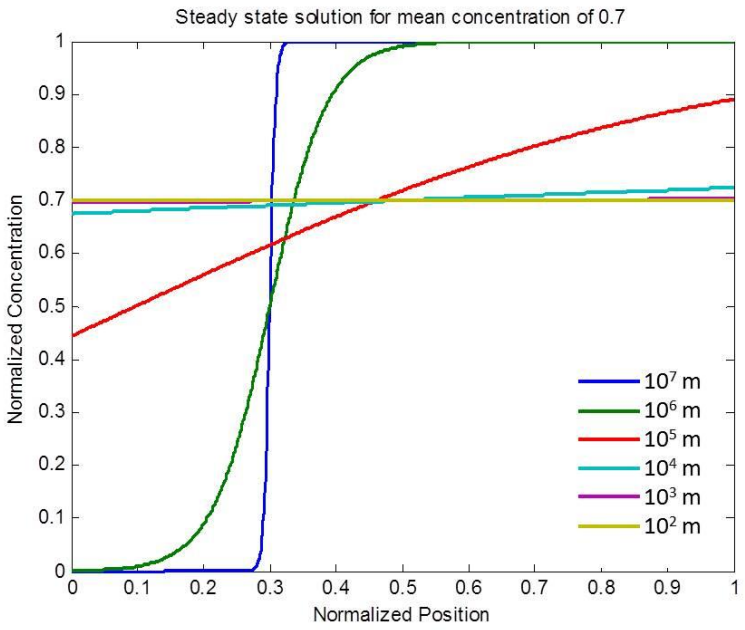

Figure 5: Normalized ion concentration profiles for devices of varying length with the same applied voltage

These ion distribution profiles reproduce theoretical and experimental results at the two extremes in device length. First, nanoscale memristors with 100 nm length scales have been theoretically predicted [10] and experimentally shown [37] to have a discrete boundary between a conductive region and an insulating region rather than a continuous distribution of ions. This feature is demonstrated in Figure 5. In contrast, macroscale memristors were theoretically predicted to have a continuous distribution of ions that is linear in steady state conditions [52]. *In situ* X-ray absorption measurements of macroscale memristors have experimentally demonstrated a continuous distribution of states [59].

Before we can apply these ion motion relationships to memristors, we must first define the internal state variables of the memristor, the electrical and thermal

characteristics which result in activated ion motion, such that we can subsequently link the state variables to the ion motion.

3.4 *Characteristic Equation Model*

Chua's 1976 memristive system is described by the set of equations 3.15 – 16, where $\vec{u}$, $\vec{y}$, and $\vec{x}$ are respectively the system input, the system output, and an internal state variable and functions f and g are arbitrary [20]. These three variables are generally vector quantities allowing for multiple inputs, multiple outputs, and multiple internal mechanisms. This formalism provides a framework to describe multi-functional memristive devices that can be controlled electrically, thermally, chemically, optically, or magnetically.

$$\frac{d\vec{x}}{dt} = f(\vec{x}, \vec{u}, t) \qquad \text{Equation 3.15}$$

$$\vec{y} = g(\vec{x}, \vec{u}, t) * \vec{u} \qquad \text{Equation 3.16}$$

While the mathematical, state variable description for a memristor provides no insight into the physical mechanisms behind a real device, mixed ion-electron conductors (MIEC) have demonstrated a rich set of behaviors including energy storage, rectification, negative differential resistance, and memristive hysteresis [60, 61]. In general, the kinetics of atomic motion are governed by ionic hopping conductivity [61] thermally activated according to an Arrhenius relation, as shown in Equation 3.5. Shown in Table 1 are a variety of MIEC memristors and their associated activation energies for ion motion.

Table 1: Activation Energies for Several Memristive Materials

Material	Activation Energy	Volatile	Reference
$Pr_{0.7}Ca_{0.3}MnO_3$	0.4 eV	Yes	[62]
$LiNbO_2$	0.3 eV	Yes	[63, 64]
TiO_2	>2 eV	No	[65]
Ta_2O_5	>2 eV	No	[66]

To develop a mathematical model for mixed ion-electron memristors, we begin with the general system of equations for a memristive device, Equations 3.15 – 3.16, informed by the ion hopping kinetics previously developed, Equations 3.9 – 3.12. We define the input to the system as the applied voltage V and the output of the system as the current through the device I. The specific physical state variable parameters replacing the generalized state variables in Chua's formalism, $\vec{x}$, are the scalars φ, representing the distribution of ions, and the temperature T. Rewriting Equations 3.15 – 3.16 with the above variables yields Equations 3.17 – 3.19.

$$I = G(\vec{x}, V, t) * V = G(\varphi, T, V, t) * V \qquad \text{Equation 3.17}$$

$$\frac{d\vec{x}}{dt} = f(\vec{x}, V, t) = f(\varphi, T, V, t) \qquad \text{Equation 3.18}$$

$$\vec{x} = \begin{bmatrix} x_1 \\ x_2 \end{bmatrix} = \begin{bmatrix} \varphi \\ T \end{bmatrix} \qquad \text{Equation 3.19}$$

where G is function describing the device conductance and t is time. Looking first at the state variable dynamics, Equation 3.18, the temperature of the device can be easily approximated by the differential Equation 3.20 that balances Joule heating and conductive heat transfer.

$$\frac{dx_2}{dt} = \frac{dT}{dt} = \frac{1}{m*C} * \left[G * V^2 - \frac{k*A*(T-T_E)}{\Delta L} \right] \qquad \text{Equation 3.20}$$

Equation 3.20 is the result of thermal energy input to the device by Joule heating and conductive heat transfer removing heat from the device along a thermal length. The device's temperature change is governed by the total heat capacity. The variables involved are: m is the mass of the device, C is the material's specific heat capacity, V is the applied voltage, k is the thermal conductivity, A is the surface area of the device, T_E is the temperature of the environment, and ΔL is the length for thermal transfer. The first

term in the brace describes Joule heating while the second term is the conductive heat loss. No explicit device geometry is defined for this generalization, but various geometries can be approximated by changing the mass, surface area, and thermal transfer length.

While the temperature dynamics can be derived from basic physical relationships, the specific dynamics of the ion distribution state variable φ will depend generally on the internal physics of the modelled device. For example, in devices with small dimensions where the ion distribution displays a clear transition between two regions, as shown in Figure 5, the ion distribution state variable may be selected to represent the position of the transition. However, it will be shown that the rich behavior of memristive devices can be described by the ion distribution state variable dynamics shown in Equation 3.21.

$$\frac{dx_1}{dt} = \frac{d\varphi}{dt} = A * V - D * \varphi \qquad \text{Equation 3.21}$$

A is a parameter dependent on device geometry (i.e. scaling of voltage to electric field), but in more complex implementation can encompass many other physical effects that relate the external applied voltage to the change in ion distribution. A is thus a generalized parameter describing the strength of the applied voltage V on the ion distribution state variable. Likewise, D describes the strength of ion distribution recovery accounting for physical effects such as diffusion. The ion distribution state variable dynamics, Equation 3.21, build on earlier models that include the first voltage driven term but neglect any recovery mechanisms [10]. It should be noted that the ion distribution state variable, φ, cannot be explicitly defined outside the context of a specific device geometry and as such the units of φ, A, and D are not yet definable.

In general, the coefficients A and D can be functions of many variables. However, because they describe the ease of ion motion, both coefficients must follow an Arrhenius relationship and thus, from Equations 3.9 – 3.10, account for the ion motion activation energy shown in Equation 3.22.

$$A, D \propto e^{-\frac{E_A}{kT}} \qquad \text{Equation 3.22}$$

Examining Equation 3.21, it is clear that in the steady state when there is no net ion movement (i.e. $\frac{d\varphi}{dt} = 0$), the voltage driven term and distribution recovery term must balance. This limits the extent of the ion distribution state variable placing a maximum value on φ, shown in Equation 3.23, for a given maximum voltage V_{max}.

$$\varphi_{max} = \frac{AV_{max}}{D} \qquad \text{Equation 3.23}$$

It should be noted that A and D are not in general time-independent as they depend upon thermal activation. However, for small thermal fluctuations, assuming time-independent values for A and D, the dynamics the ion distribution state variable, φ, can be obtained by integrating Equation 3.21 to yield Equation 3.24, which is a Volterra equation of the second kind with a solution given by Equation 3.25.

$$\varphi(t) = A\int_{-\infty}^{t} V(\tau)d\tau - D\int_{-\infty}^{t} \varphi(\tau)d\tau \qquad \text{Equation 3.24}$$

$$\varphi(t) = A\phi(\mathrm{t}) - \mathrm{D}\int_{-\infty}^{t} e^{-D(t-\tau)}\phi(\tau)d\tau \qquad \text{Equation 3.25}$$

Where ϕ is the time integral of voltage (flux-linkage) given in Equation 2.1b.

Further, the second term of Equation 3.25 can be recognized as the convolution between the flux-linkage and a decaying exponential. Therefore, the frequency dependence of the ion dynamics Equation 3.21 can be described by the Fourier transform

given in Equation 3.26, which is a first order filter with critical frequency ω = D. At this critical frequency a maximum in the reactance occurs.

$$F\{\varphi(t)\} = F\{\phi(t)\}\left[A - \frac{D}{D+j\omega}\right] \qquad \text{Equation 3.26}$$

Where F is the Fourier transform operator and j is the square root of -1.

Finally, while the ion motion is controlled by the activation energy and available thermal energy, the conductivity of the device is controlled by the available electrons (or holes) and their distribution. The exact form of the device conductivity as a function of ion distribution G(φ) will depend on the specific memristor. Equations 3.17, 3.20, and 3.21 combined forms a set of equations that fully describe memristor behavior, specifically, the conductance, thermal response, and the associated thermally activated hopping motion of ions. The task for modelling memristors of differing underlying physics is then to define A, D, and a functional relationship between G and φ. Chapter 4 provides two diverse examples spanning experimentally demonstrated extremes in memristor behavior. First demonstrated is a nanoscale non-volatile filamentary memristor based on TiO_2 and second, a macroscale volatile memristor based on $LiNbO_2$.

CHAPTER 4

MEMRISTOR MODEL EXAMPLES

4.1 *Nanoscale Non-volatile Filamentary Memristor*

Non-volatile filamentary memristors have been well characterized since their discovery in 2008 [10] and have been modelled numerous ways to account for ion drift [10], electrochemical potential [50], ion boundary conditions [53], and multiple filaments [54] among many other effects.

While the internal state variable for filamentary memristor models is typically chosen as the normalized filament length [10], confining this variable to a limited set of values , i.e. a domain from 0 – 1, leads to difficulties near the device boundaries requiring window functions or other numerical methods in order to bring the filament speed to zero and keep the modeled filament within the device [53]. Alternatively, the state variable can be projected onto an infinite domain such that the window function becomes incorporated into the projection. While the physics governing the filament speed as it approaches a contact is yet unknown, the filament is assumed to asymptotically decelerate as it approaches a contact. Whatever function is chosen to model this effect should reflect the asymptotic slowing of the filament as it approaches the contact. Such a function is given in Equation 4.1 as a hyperbolic tangent.

$$w(\varphi) = \frac{1+\tanh(c*\varphi)}{2} \qquad \text{Equation 4.1}$$

Where w is the original domain limited state variable (normalized filament length) asymptotically constrained to the accepted values (0 – 1), φ is the state variable projected onto an infinite domain, and c is a scaling parameter equal to 2 so as to match

w to φ (dw/dφ = 1) away from the device edges. With this transform, the traditional filamentary memristance equation [10], shown in Equation 4.2, can then be used directly with the original state variable.

$$G = \frac{1}{R_{ON}w + R_{OFF}(1-w)} \qquad \text{Equation 4.2}$$

Where R_{ON} is the resistance of a fully formed filament and R_{OFF} is the resistance with no filament formation.

For this example, with the state variable defined as a projection of the filament length, the ion dynamics Equation 3.21 becomes a scaled filament edge speed far from the boundary edges that is asymptotically reduced to zero as the edges are approached, and can be found from the time derivative of Equation 4.1 as shown in Equation 4.3.

$$\frac{d\varphi}{dt} = \frac{2}{c} * \cosh^{-2}(c\varphi) * \frac{dw}{dt} \qquad \text{Equation 4.3}$$

This filament speed can be considered as the motion of ions making up the filament. Thus, the filament speed can be considered analogous to the ion current making the first term of Equation 3.21 equivalent to a drift term and the second term equivalent to diffusion. This allows the ion dynamics to be defined by Equations 4.4 – 4.5, where the drift and recovery coefficients are related by the Einstein relationship. The Einstein relationship is only appropriate away from the contacts where the ion distribution state variable, φ, is nearly linear with the filament length. Near the contacts, the non-linear projection dominates the recovery term and approximates the unknown effects that confine the filament to the device.

$$A = \mu_V S c_{eff} e^{-\frac{E_A}{k_B T}} \qquad \text{Equation 4.4}$$

$$D = \frac{1}{c_{eff}} \frac{k_B T}{q} A \qquad \text{Equation 4.5}$$

Where μ_v is the mobility of the filament ions, the constant S is a geometric factor with units of inverse length, and T is the temperature calculated in Equation 3.20. The geometric factor serves to convert the terminal voltage into an appropriate internal electric field. The effective number of free sites for hopping conductivity, c_{eff}, modifies both the drift and diffusion terms as shown in Equations 3.10 – 3.12. As previously stated, the local electric field in a filamentary memristor during switching is likely high enough to forbid the use of the linear ion hopping equation. To account for the high field mobility encountered during switching, an effective mobility, orders of magnitude higher than would be otherwise expected, is used instead. For example, by comparing the effective field-dependent mobility from Equation 3.5 with the low field mobility from Equation 3.10, a discrepancy of order 10^{15} – 10^{31} occurs at fields between $1x10^9$ – $2x10^9$ V/m. As shown in Table 2, the expected low field mobility, on the order 10^{-4} cm^2/V-s, is multiplied by a constant factor to account for the high field effective mobility. This method was chosen over a true non-linear mobility in order to maintain the model simplicity for large scale circuit simulations.

Two simulations of a TiO_2 filamentary memristor were performed using the parameters listed in Table 2 and a sinusoidal driving force reproducing several experimental observations. While the physical, thermal, and electrical parameters are identical, the two simulations differ in the activation energy necessary for oxygen ion motion and changes in ion mobility necessary to observe switching in diversely different activation energy devices. Case 1 closely resembles the non-volatile TiO_2 memristor with essentially no ion relaxation over roughly 30 years, while case 2 is a fictional case for comparison purposes with relaxation (volatility) on the order of milliseconds.

Table 2: Simulation Parameters for a TiO_2 Memristor.

		Case 1	Case 2
Physical Parameters	Device radius (r): Device length (L): Density:	10 nm 50 nm 4.23 g/cm^3	10 nm 50 nm 4.23 g/cm^3
Thermal Parameters	Specific Heat (C): Thermal conductivity (k): Thermal length (ΔL):	0.693 J/g-K 0.117 W/cm-K r/2	0.693 J/g-K 0.117 W/cm-K r/2
Electrical Parameters	R_{ON}: R_{OFF}:	200 Ω 2000 Ω	200 Ω 2000 Ω
Ion Parameters	u_V: S: c_{eff}: E_A:	$10^{-4}*10^{21}$ cm^2/V-s 1/L 0.1 2 eV	$3x10^{-4}*10^{12}$ cm^2/V-s 1/L 0.1 0.5 eV
Driving Force	$V_{Applied} = \cos(2\pi f t)$ $f = 1\ MHz$		

Data found in references [10, 37, 40]

As shown in Figure 6a-b, both cases reproduce the experimentally observed bow-tie I-V curve with dynamic negative differential resistance upon switching [10]. In general, the abrupt turn on of a high activation energy material, Figure 6a, is softened when the activation energy is lower, as in Figure 6b. In principle, if the thermal characteristics were known, the activation energy of the material could be extracted from fitting the I-V curve. Figure 6b shows an initial transient resulting from the initial condition of the filament length. This initial transient is not a strong effect in the high activation energy case because ion motion does not occur until substantially higher temperatures compared to that of the lower activation energy case. This is seen in the average temperature of the devices which differ by over 200 ^{o}C.

Examining the temperature of the device, shown on the color scales of Figure 6 and plotted versus time in Figure 7a-b, the simulation reproduces the asymmetric time spent in the high versus the low resistance state as previously observed [10]. Specifically, as shown by the shaded areas in Figure 7, the device spends less time in the low

conductance state, shaded in blue, and more time in the high conductance state, shaded in red. In addition, by including the thermal activation of ion motion, the 2 eV activation energy case accurately predicts the onset of switching when the device is between 600 K and 900 K agreeing with more complex finite element models [39]. Finally, the switching time between the two conductance states is simulated at 70 ns, again closely matching experimental observations [67].

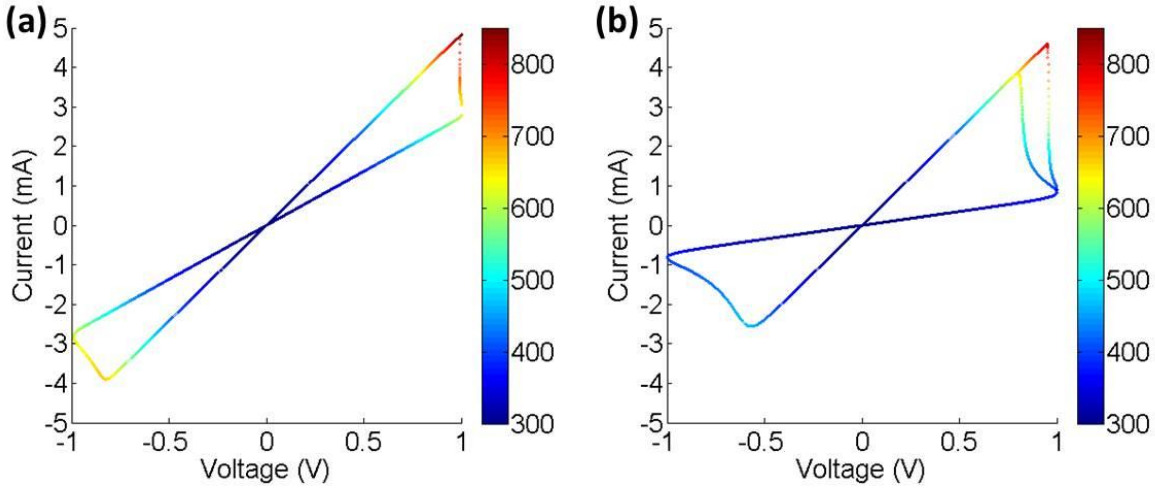

Figure 6: Simulated current – voltage characteristics of a non-volatile filamentary memristor with (a) a 2 eV activation energy barrier to ion motion and (b) a 0.5 eV activation energy barrier to ion motion.

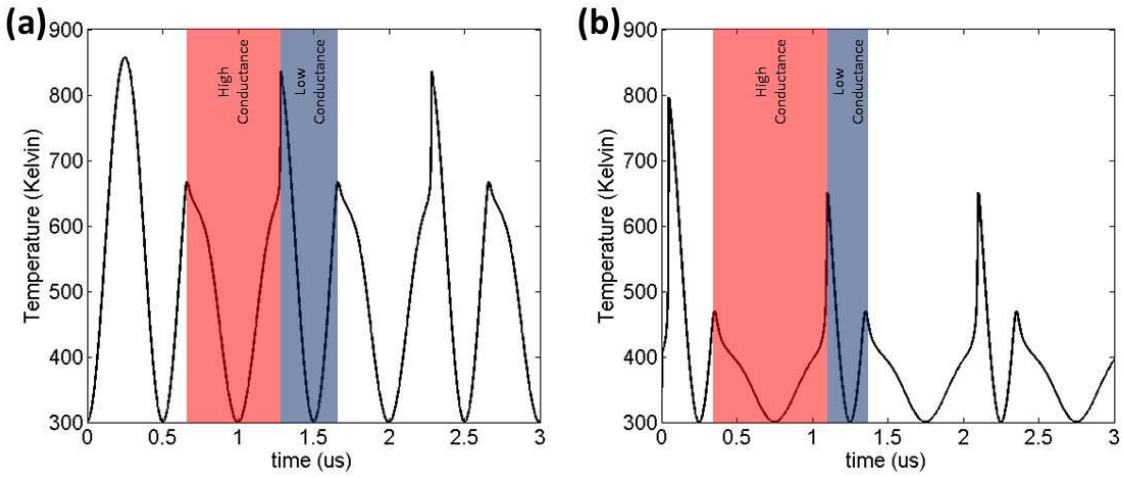

Figure 7: Temperature simulations of a non-volatile filamentary memristor with (a) a 2 eV activation energy barrier to ion motion and (b) a 0.5 eV activation energy barrier to ion motion. Switching

occurs at elevated temperatures with the time spent in the high conductance state highlighted in red and the time spent in the low conductance state highlighted in blue.

Thus, by defining the TiO_2 non-volatile memristor state variable to be the filament length and projecting this state variable onto an infinite domain explicitly including the activation energy necessary for ion motion reproduces several important experimentally observed switching behaviors in a compact device model. This simple model avoids boundary value problems encountered in other finite domain models and explicitly includes the temperature dependence of memristive switching. Additionally, the predicted temperature for switching is in the same range as previous complex finite element models [39] and could be used in complex circuit simulations to predict heat dissipation and thermal crosstalk between nanoscale devices. As will again be seen below, the value of the ion motion activation energy is the controlling factor as to whether a device is volatile or non-volatile. Thus, by including a lower activation energy for ion motion, the proposed simple model can also be applied to volatile memristors.

4.2 *Macroscale Volatile Memristor*

In contrast to the well characterized non-volatile filamentary memristors, volatile memristors are less well known but can be useful for mimicking the natural volatility of a neural system. In addition, due to the lower activation energy for ion motion and the lack of filamentary behavior, volatile memristors have been observed on discrete devices with millimeter length scales [43]. As memristive effects increase with decreasing length scales, shown in Equation 4.6 [10], these devices have enormous potential for low power nanoscale memristors.

$$M(x) \propto \frac{1}{L^2} \qquad \text{Equation 4.6}$$

Due to memristive effects scaling with the inverse square of the length, a three order of magnitude decrease in the length scale (100 um to 100 nm) theoretically permits the same memristive behavior with a six order of magnitude decrease in the driving input (1V to 1uV). Therefore, while the analog device modelled herein is a large device (100 μm length matching experimental reports [58]) representing an extreme upper bound for the model to consider, the scaled down version of this device should be capable of operation at lower power and with larger memristive hysteresis.

Unlike the non-volatile device which has normalized filament length as a state variable, the physics of the $LiNbO_2$ volatile memristors are not dependent on the formation, destruction and movement of filaments. Instead, for the $LiNbO_2$ volatile memristor the internal state variable is based on the continuous ion distribution. Finite element models of the $LiNbO_2$ memristor [52] show transient complex ion distributions and the resulting conductance. However, in all cases, at slow excitation or in steady state, the complex ion distributions collapse into a steady state linear ion distribution and an associated conductance. In these materials operated in electric fields from 10^1 to 10^5 V/m, the linearized mobility model is certainly valid. Given this linear ion distribution and its associated conductance state, one can easily connect the ion distribution (a slope in steady state) to the conductance, G, and again connect that conductance to the flux-linkage, φ, through the use of the current-voltage curve.

Examining experimental data, shown in Figure 8, from a large scale volatile $LiNbO_2$ memristor, the characteristic pinched hysteresis of a memristor is observed. This data was measured at 42 mHz on a lateral ring-dot structure with asymmetric contact areas and a device length of 55 μm.

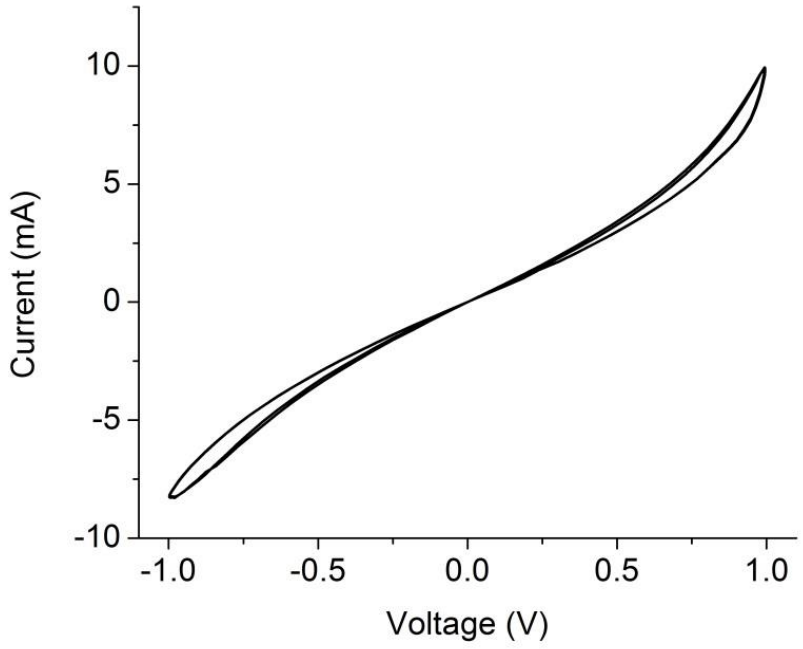

Figure 8: The experimental current – voltage relation for a volatile $LiNbO_2$ memristor measured at 42 mHz.

Since the conductance of the device is known from the slope of the current-voltage curve for each time point and the flux-linkage can be determined as the time integral of the voltage, one can plot the experimental data in Figure 8 as a conductance versus flux-linkage as shown in Figure 9. The flux linkage represents the combined effects of an applied voltage and the time the voltage has been applied making small voltages applied for long times as effective as large voltages for short times. In Figure 9, two conductance values at zero φ and asymmetric shape around zero φ are apparent. This asymmetry in the experimental data is likely due to asymmetric contacts on the ring-dot structure and is not accounted for in the following model. Such effects have been accounted for in previous finite element models [52].

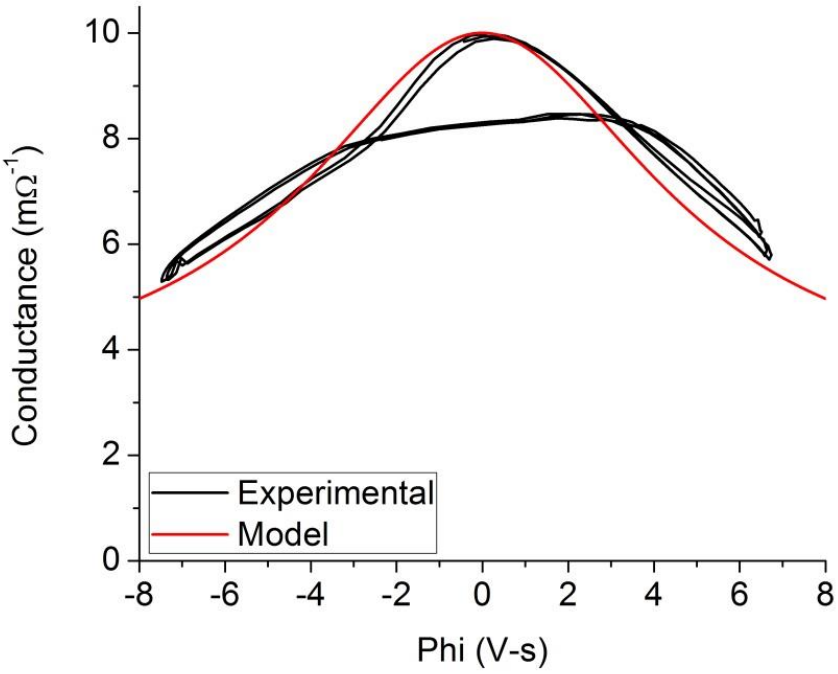

Figure 9: The experimental Conductance – Phi relation from a $LiNbO_2$ memristor and the fit used to model the device. The two values at Phi = 0 are due to the asymmetric contact geometry of the experimental device. By modelling only one contact geometry a symmetric device is modelled.

Fitting the experimental data for one of the contact polarities, which forces a symmetric response, the following conductance, shown in Equation 4.7, was empirically fit to the experimental volatile memristor conductance.

$$G(\varphi) = G_L - \frac{G_L - G_H}{1+(c\varphi)^2} \qquad \text{Equation 4.7}$$

Where G_H = 0.01 Ω^{-1} is the high conductance state, G_L = 0.005 Ω^{-1} is the low conductance state, and c = 0.2 is a width parameter used to fit the experimental data.

For steady state simulations, it has been shown that the ion concentration profile, N(x), in these volatile memristors is linear [52]. However, a linear ion distribution is incompatible with the current continuity equation when simplifications are made that are necessary for a simple model compatible with large scale circuit applications. Such simplifications

include a uniform electric field and a negligible space charge due to ion-electron separation (i.e. quasi-neutrality). The linear ion distribution incompatibility arises because the derivative of the current density (dJ/dx) does not include a diffusion term necessary to balance the drift term and bring the ion motion (dN_{Li}/dt) to zero as shown in Equation 4.8.

$$\frac{dN}{dt} = -\frac{1}{q}\frac{dJ}{dx} = -\frac{1}{q}q\mu_{Li}\frac{dN}{dx}E \neq 0 \qquad \text{Equation 4.8}$$

This non-physical result is likely due to the two assumptions above. At long time scales the electrons and ions separate violating quasi-neutrality and setting up an electric field opposing the applied field. However, for shorter time scales, a transient ion distribution occurs [52] that is modelled herein as a cubic ion distribution profile as shown in Equation 4.9.

$$N(x) = N_o + \gamma(t)\left(x - \frac{L}{2}\right) + \lambda(t)\left(x - \frac{L}{2}\right)^3 \qquad \text{Equation 4.9}$$

The cubic distribution does not violate the current continuity equation and can thus be modelled simply as shown in Equation 4.10.

$$\frac{dN}{dt} = -\frac{1}{q}\frac{dJ}{dx} = \mu_{Li}\frac{dN}{dx}E - qD_{Li}\frac{d^2N}{dx^2} \qquad \text{Equation 4.10}$$

Taking the first and second derivatives of Equation 4.9 and inserting them into Equation 4.10 yields Equation 4.11.

$$\frac{dN}{dt} = \mu_{Li}\left(\gamma(t) + 3\lambda(t)\left(x - \frac{L}{2}\right)^2\right)E - qD_{Li}\left(6\lambda(t)\left(x - \frac{L}{2}\right)\right) \qquad \text{Equation 4.11}$$

Because γ(t) and λ(t) are of the same order of magnitude for the modelled devices and the length scale is one the order of 10^{-2} cm, the second drift term is much smaller than the first drift term and may be dropped. This simplification yields Equation 4.12.

$$\frac{dN}{dt} = \mu_{Li}\gamma(t)E - 6qD_{Li}\left(x - \frac{L}{2}\right)\lambda(t) \qquad \text{Equation 4.12}$$

At long time scales the ion distribution becomes linear and the cubic term in the ion distribution, λ(t), presumably goes to zero. However, for faster time scales the linear term γ(t) is nearly constant and the cubic term becomes the dominant time dependent term. An estimate for the frequency at which this transition occurs can be determined from previous finite element models that examine the step response of $LiNbO_2$ memristors. Previous models have shown that for a device with order 1 um length, a cubic profile is present 0.1 sec after the voltage step, but a linear profile is present after 1 sec [52]. Scaling these times for the 100 um device modelled herein, it is expected that the cubic approximation can be made for time scales shorter than 10 seconds or faster than 0.1 Hz. This is consistent with experimental results testing the step response of $LiNbO_2$ memristors [42]. Thus for the time scales of interest to neuromorphic computing (0.1 – 100 Hz) the linear term can be treated as effectively constant, γ(t) ≈ γ, and the cubic term is the dominant time dependent term in the ion motion. Taking the time derivative of the ion concentration under this assumption yields Equation 4.13.

$$\frac{dN}{dt} = \frac{d\lambda(t)}{dt}\left(x - \frac{L}{2}\right)^3 \qquad \text{Equation 4.13}$$

Evaluating the change in ion concentration at the contact (x = L) and setting Equation 4.12 and Equation 4.13 equal, we then obtain the dynamics Equation 4.14.

$$\frac{d\lambda(t)}{dt} = \mu_{Li}\gamma\left(\frac{L}{2}\right)^{-3} E - 6D_{Li}\left(\frac{L}{2}\right)^{-2}\lambda \qquad \text{Equation 4.14}$$

This dynamical equation follows the same form as Equation 3.21 allowing the assignment of the ion distribution state variable, φ, to be the cubic ion distribution term, λ. Thus the ion dynamics can be written as Equations 4.15 – 17.

$$\frac{d\varphi}{dt} = \left[\frac{8\mu_{Li}\gamma}{L^4}\right]V - \left[\frac{24D_{Li}}{L^2}\right]\varphi = AV - D\varphi \qquad \text{Equation 4.15}$$

$$A = \frac{8\mu_{Li}\gamma}{L^4}$$ Equation 4.16

$$D = \frac{24D_{Li}}{L^2}$$ Equation 4.17

The simulated result, shown in Figure 10, matches the experimental results except at negative voltages where the change from an asymmetric to a symmetric device becomes apparent.

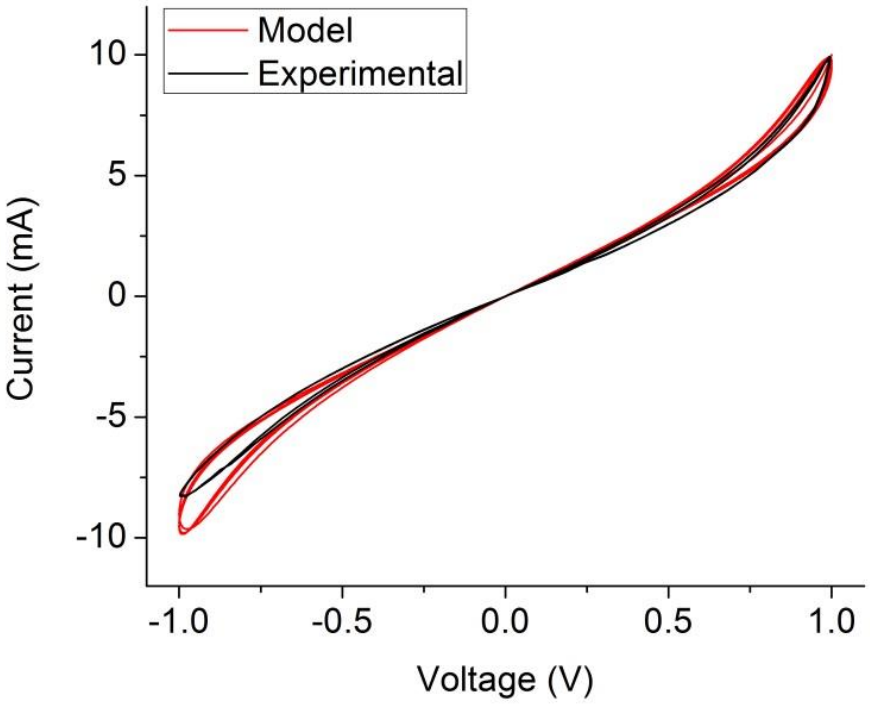

Figure 10: Simulated and experimental current – voltage relation of a volatile memristor based on $LiNbO_2$. Deviation between the modelled and experimental results at negative voltages is due to the asymmetric geometry of the experimental device, which was not considered for the model.

In addition, the activation of ion motion by thermal energy is not necessary for low activation energy volatile memristors, and the temperature of the simulated device varies by less than 1^oC as shown in Figure 11.

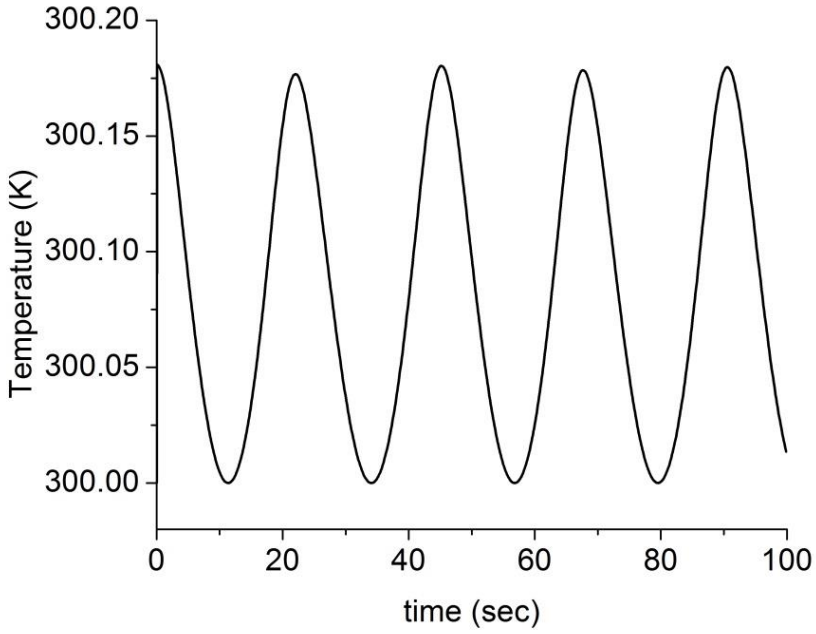

Figure 11: The temperature of a simulated volatile memristor showing effectively room temperature operation.

It was theorized that for memristive mobile ion-electron conductors (MIECs), a decrease in frequency would lead to a current-voltage relation with peaks as the mobile dopants redistribute [60]. This effect is reproduced, as shown in Figure 12, using the same simulation parameters as in the volatile memristor example, by decreasing the frequency one order of magnitude. It should be noted that this current-voltage relation is distinctly different than that for the filamentary memristor, which also exhibits a peak with dynamic negative differential resistance. The difference arises near the origin where a filamentary memristor's current-voltage relation crosses at the origin, but a volatile memristor's current-voltage relation is pinched at the origin. The peaks in the volatile memristor current-voltage curve result from diffusion assisted ion recovery returning the ion gradient to zero before the voltage reaches the maximum value. When the ion gradient (φ) is zero, the conductance is maximized as shown in Figure 9.

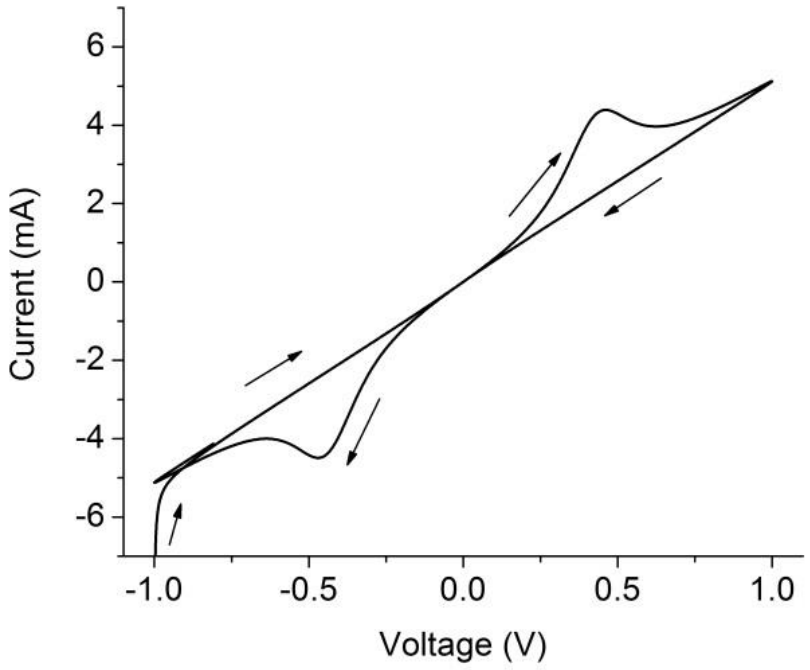

Figure 12: Simulated current – voltage relation for a volatile memristor at low frequency exhibiting dynamic negative differential resistance as ionic diffusion returns the ion gradient to zero before the voltage reaches a maximum.

This dynamic negative differential resistance has been experimentally observed in $LiNbO_2$ volatile memristors. As shown in Figure 13 for a single current-voltage sweep, a peak in current occurs before the voltage reaches its maximum value. In addition to the dynamic negative differential resistance, both the simulation, Figure 12, and the experimental data, Figure 13, show an initial increase in resistance as the voltage sweep begins at -1 volt. This initial transient effect is caused by the maximum (in magnitude) voltage (-1 V) occurring at the same time as the maximum conductance state resulting from $V \cdot t=0$ in Figure 9. This condition does not occur again after the initial condition because the diffusion assisted ion recovery creates a phase offset between the maximum voltage and flat ion distribution as theoretically derived in Equation 3.26.

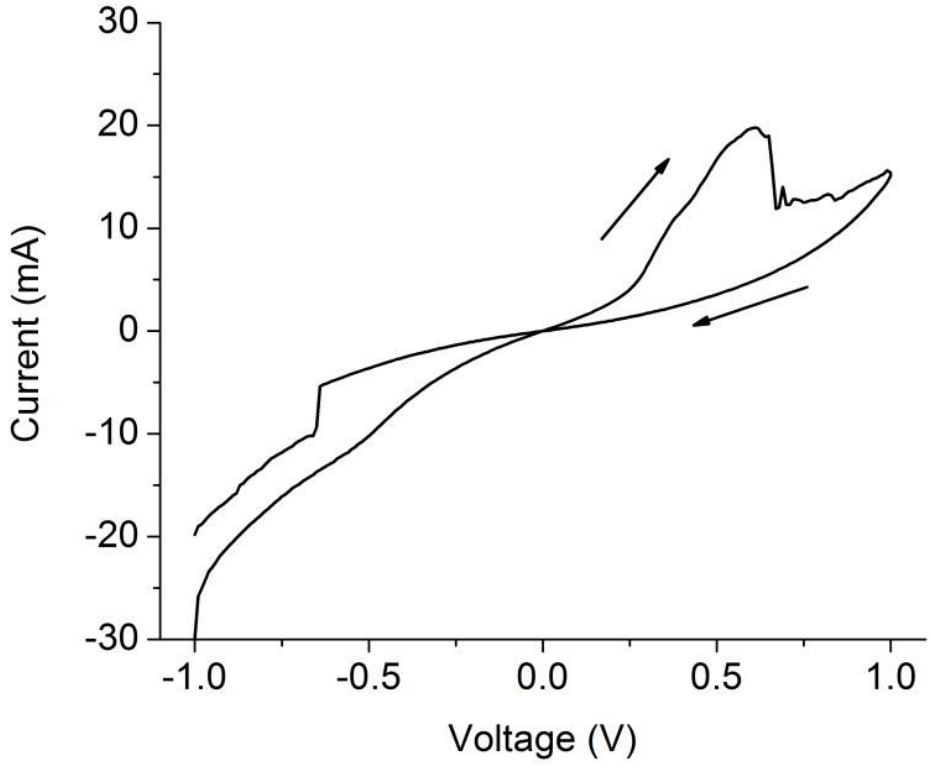

Figure 13: Experimental data showing dynamic negative differential resistance and an initial high conductance transient.

CHAPTER 5

APPLICATIONS OF VOLATILE MEMRISTORS IN NEUROMORPHIC COMPUTING

5.1 *Schmitt Trigger – Spike Frequency Adaptation*

The device models discussed in Chapter 4 are computationally simple while still incorporating physical parameters such as geometry and dopant levels that can be used to modify parameters such as the device speed and the magnitude of the memristance change. However, these devices do not necessarily implement important neuromorphic functions on their own. An example is given below in which biologically realistic spike-frequency adaptation is implemented in a simple Schmitt Trigger circuit by replacing one of the resistors in the Schmitt Trigger's voltage divider with a volatile memristor. The ionic integration built into the dynamics of the memristor creates an adaptive level shifter, adding new dynamics to the circuit as a whole without increasing the circuit complexity.

Previously a non-volatile memristor with external programming circuitry was included in an op-amp Schmitt Trigger to create a variable threshold Schmitt Trigger [68]. The circuit presented in Figure 14 differs from this previous work in two ways that are important for neuromorphic circuit applications. First, the memristor implementation is a volatile analog memristor rather than a non-volatile filamentary memristor. Second, the circuit presented is self-programming and requires no external programming controller. This leads to a higher computational density. These distinctions make it useful for neuromorphic spike-frequency adaptation.

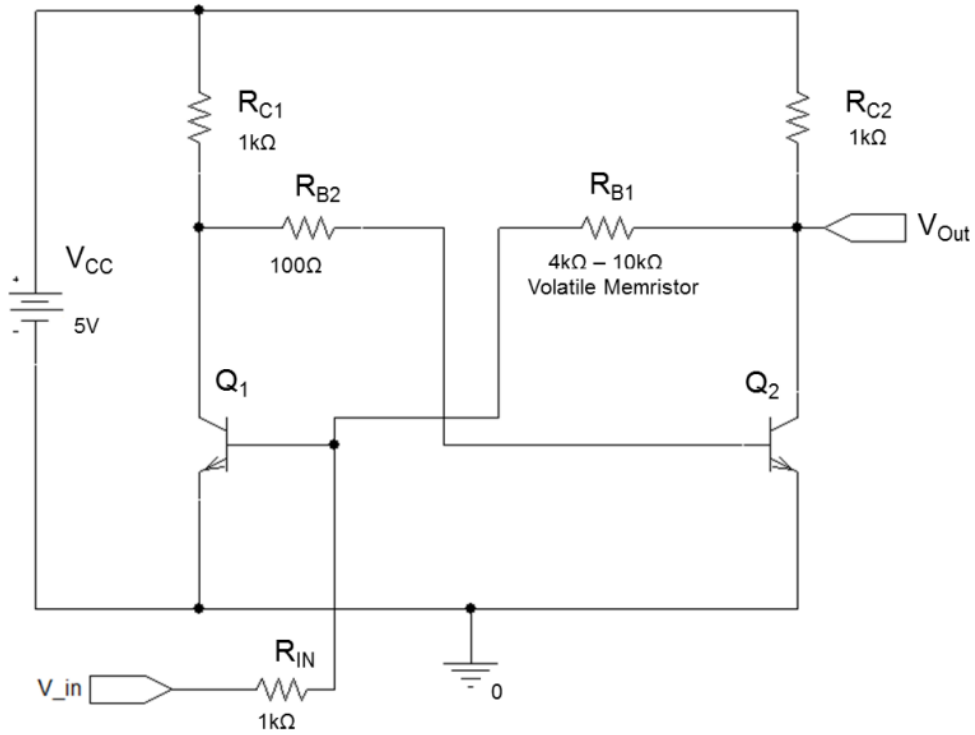

Figure 14: A collector-base coupled BJT Schmitt Trigger circuit diagram with a volatile memristor substituted for resistor R_{B1}.

The circuit shown in Figure 14 is a classical collector-base coupled BJT Schmitt Trigger. Advantages of this design for a neuromorphic threshold detector are a near zero low-output voltage and a high-output voltage set by the voltage divider R_{C2}, R_{B1}. These two attributes provide a near ground output and an adaptable high state output for the analog spike generation circuit this Schmitt Trigger controls.

The BJT Schmitt Trigger circuit works as follows: while V_{in} is below the rising threshold, transistor Q1 is off and Q2 is on. The output voltage is tied to ground through transistor Q2. The base-emitter voltage of Q1 is set by the voltage divider R_{in}, R_{B1} and the rising threshold occurs when this voltage divider forward biases the base-emitter junction of Q1.

After transitioning to the high-output state, transistor Q1 is on and Q2 is off. The output voltage is set by the voltage divider R_{C2}, R_{B1}. As V_{in} decreases, the falling threshold occurs when the base of Q1 is deprived of current. This requires the current through R_{B1} to equal the current through R_{in}. Assuming ideal BJTs, these thresholds and outputs are given by Equations 5.1 – 5.4.

$$V_{T\uparrow} \approx \frac{(R_{in}+R_{B1})V_{BE}}{R_{B1}} \quad \text{Equation 5.1}$$

$$V_{T\downarrow} \approx V_{BE} - \frac{R_{in}(V_{cc}-V_{BE})}{R_{B1}+R_{C2}} \quad \text{Equation 5.2}$$

$$V_{Out-Low} \approx 0 \quad \text{Equation 5.3}$$

$$V_{Out-High} \approx \frac{R_{B1}(V_{cc}-V_{BE})}{R_{B1}+R_{C2}} \quad \text{Equation 5.4}$$

Where $V_{T\uparrow}$ is the rising threshold voltage, $V_{T\downarrow}$ is the falling threshold voltage, V_{CC} is the power supply voltage, V_{BE} is the BJT base-emitter forward bias voltage and the low and high subscript on V_{Out} indicates the output voltage in the low and high state respectively.

From Equations 5.1 – 5.4 it is clear that resistor R_{B1} is crucial in setting the rising threshold, the falling threshold, and the high output voltages. Figure 15 shows the Schmitt Trigger circuit transfer function for two values of R_{B1} easily achievable with the lithium niobite memristors described in Section 4.2.

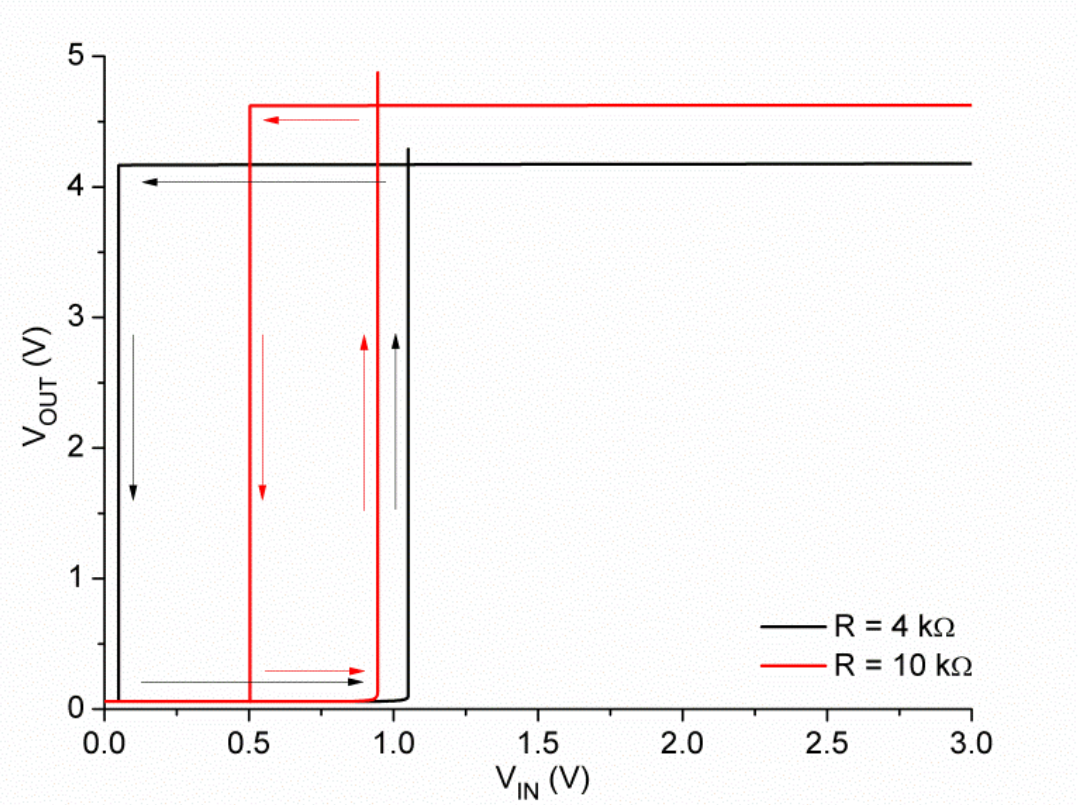

Figure 15: Changes in the Schmitt Trigger transfer function for different values of the memristor resistance including changes in the rising threshold voltage, falling threshold voltage, and high output voltage.

Changing the value of R_{B1} by only 150% changes the rising threshold by -10%, the falling threshold by 1000%, and the high output voltage by 10%. The low output voltage remains unchanged in the millivolt range. As the resistance of R_{B1} changes in Figure 15 from 10kΩ to 4kΩ, three distinct changes occur that are important for neural processing:

First, the rising threshold voltage increases. The rising threshold indicates how much input signal must be accumulated before the neuron outputs a spike. By increasing the rising threshold voltage, spikes become harder to initiate.

Second, the high output voltage decreases. A decrease in the high output voltage could be used by the spike generation circuit to implement spike-amplitude adaptation. It

is known that some biological neurons exhibit decreasing spike amplitude during bursting behavior while others show no change or more complex behaviors [69].

Third, the falling threshold decreases. This is important because the pulse width is related to the difference between the rising threshold and the falling threshold. After the Schmitt Trigger goes to the high state and initiates an output pulse, feedback must reset the input integrator. Since the Schmitt trigger can only be reset by the integrator being discharged below the falling threshold, the time that the Schmitt Trigger remains in the high state increases as the falling threshold is reduced. This increased spike time is consistent with biological spike-frequency adaptation and may also be useful for spike-shape adaptation in the spike generation circuit. For example, the "afterhyperpolarization" phase of a biological neuron spike becomes more pronounced after a high level input [69]. The increased pulse width produced by the Schmitt Trigger for high level inputs could be used in the spike generation circuit to accomplish this spike-shape adaptation.

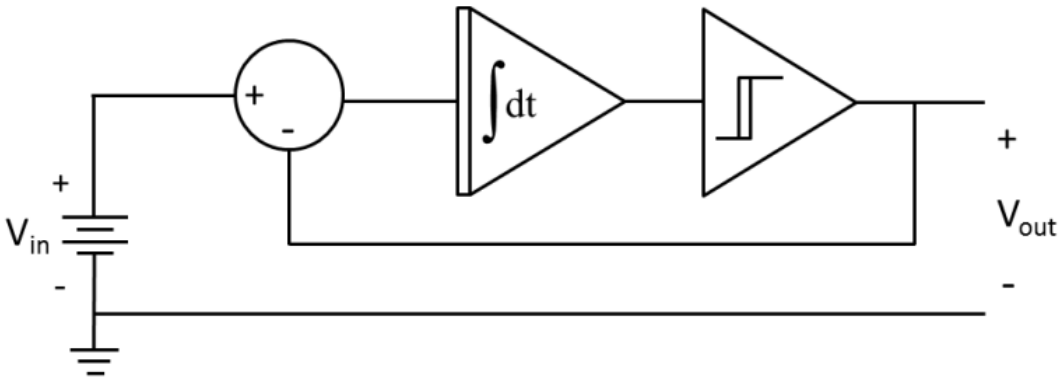

Figure 16: Diagram of a simplified neuron used to demonstrate the effects of the volatile memristor Schmitt Trigger on the overall neuron performance. The output of the Schmitt Trigger is fed back to the integrator to reset the integrator after the neuron outputs a spike.

The volatile memristor Schmitt Trigger was simulated in the simplified neuromorphic circuit shown in Figure 16. The negative feedback from the Schmitt Trigger to the integrator was used as the integrator reset mechanism.

It has been shown experimentally that for small constant inputs biological neurons produce repetitive spikes with frequencies that scale with the input value. Additionally, larger value inputs produce temporally-expanded spike widths that are sometimes accompanied by decreased spike amplitude [69]. As will be shown, this circuit mimics these biological behaviors that are thought to be crucial for biological and neuromorphic computation.

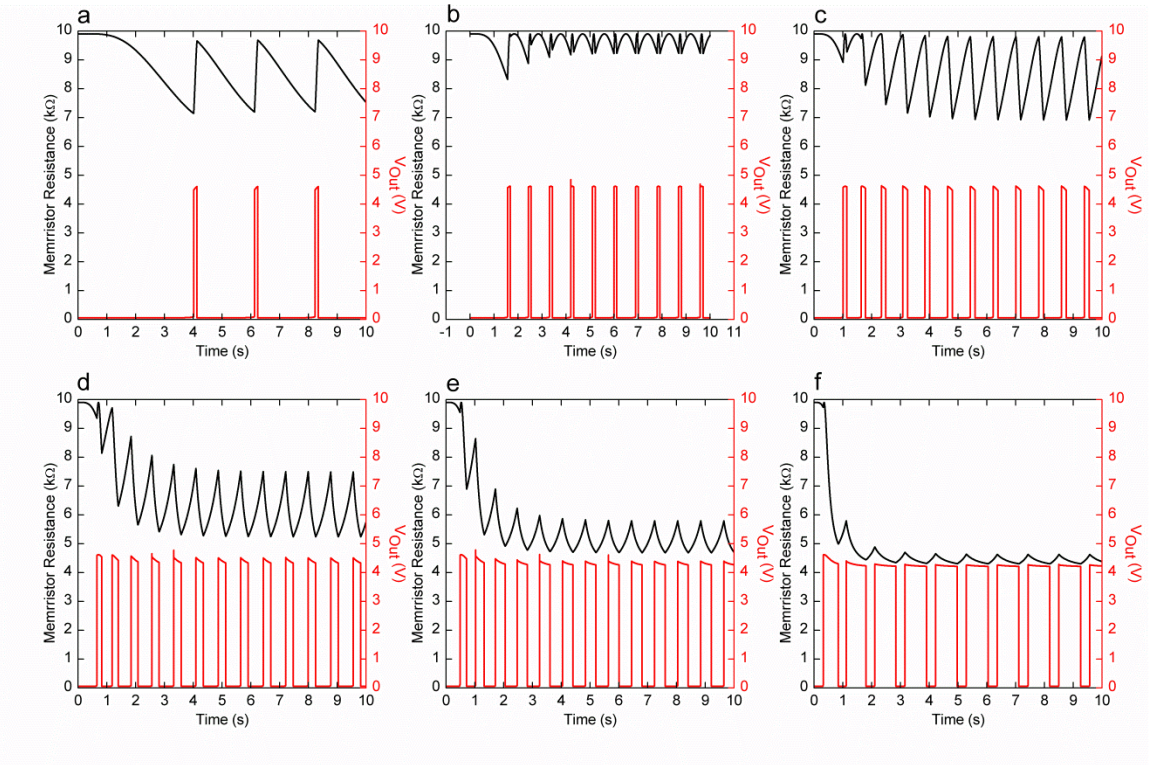

Figure 17: The output voltage and memristor resistance for six different DC input voltages to the circuit in Figure 16. The six input voltages are: a) 0.3 V, b) 0.67 V, c) 1 V, d) 1.5 V, e) 2 V, and f) 3V.

The output voltage for the volatile memristor Schmitt Trigger neuromorphic circuit is shown in red in Figure 17 for six different DC inputs. For Figure 17a-c

corresponding to smaller inputs 0.3 – 1 volts, the circuit produces repetitive pulses that increase in frequency with increasing input. In Figure 17d-f corresponding to larger inputs 1.5 – 3 volts, the output shows signs of adaptation including pulse broadening and a smooth decrease in pulse amplitude. Compared to biological pulse broadening, this simulation produced magnified results. Biological neurons broaden spikes by 20% - 100% [69] while this simulation demonstrates pulse broadening of 540%. This increased pulse broadening compared to biological spike broadening could be limited by choosing a smaller memristance change.

Examining the resistance of the volatile memristor for each of these six cases, shown in black in Figure 17, reveals why this adaptation occurs. For the small input voltages of Figure 17a-c, the memristor programming is balanced by the pulses and inter-pulse intervals so that the resistance remains near 10kΩ corresponding to the $\varphi = 0$ value in Figure 9. This allows each successive pulse to start from the same value on the $W(\varphi)$ curve. Thus, the circuit has no memory of previous pulses. For the larger inputs in Figure 17d-f, there is insufficient inter-pulse time for the memristor to fully recover back to 10kΩ and the memristor self-programs. This memory functionality of the memristor causes temporary changes in the Schmitt Trigger transfer function and thus the pulse widths and magnitudes. These changes mimic biological spike frequency adaptation.

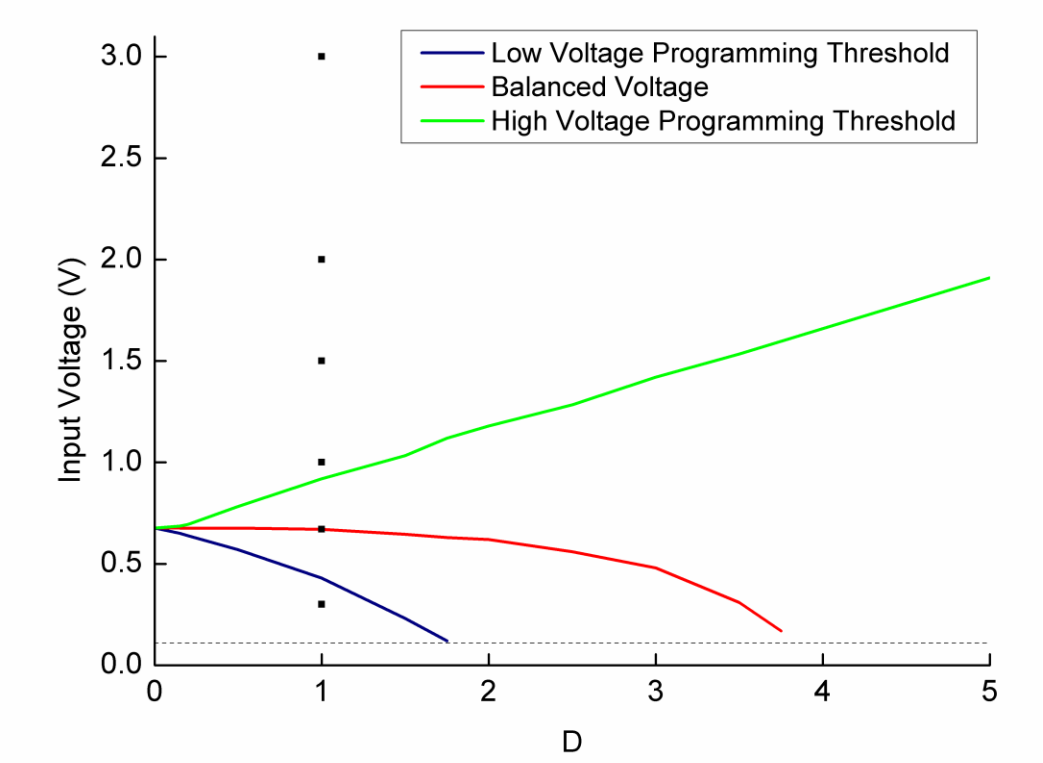

Figure 18: Three operational regimes for the Adaptive Schmitt Trigger. Input voltages below the low voltage programming threshold or above the high voltage programming threshold program the memristor producing spike frequency adaptation. Input voltages between these limits produce repetitive pulses that do not change with time.

The range of input voltages that result in adaptive and non-adaptive behavior is shown in Figure 18 where the feedback coefficient D determines the range of input values for which the memristor causes adaptation. By noting that the polarity of the voltage across the memristor switches sign for pulses versus inter-pulse time periods we see that adaptation occurs when the voltage across the memristor during each pulse is not sufficiently balanced by the restoring voltage across the memristor during the inter-pulse time. Input voltages larger than the high voltage programming threshold (green line in Figure 18) program the memristor during each output pulse because there is insufficient inter-pulse time for recovery. This condition results in spike-frequency adaptation. Likewise, inputs below the low voltage programming threshold (blue line in Figure 18)

program the memristor during the inter-pulse time. This low input programming condition is easily avoidable by choosing a sufficiently large value for D, described in Equation 4.14, making relaxation faster. The balanced voltage curve (red line in Figure 18) indicates the input voltage required to maintain a mean value of $\varphi=0$. This occurs when the pulse frequency balances programming from the pulse and the inter-pulse interval. Also shown by a dashed line in Figure 18 is the circuit activation threshold. Because the Schmitt Trigger output is subtracted from the integrator input as a reset mechanism, shown in Figure 16, inputs below the Schmitt Trigger's low state output cannot initiate a pulse. This low input "leak" effectively implements a leaky integrate and fire neuron model.

The six simulation conditions shown in Figure 17 are indicated on Figure 18 as dots. Figure 17a, V_{in} = 0.3V, is slightly below the low voltage programming threshold and Figure 17c, V_{in} = 1V, is slightly above the high voltage programming threshold. Since neither of these cases show significant adaptation, this reveals that the programming thresholds are soft thresholds defining the limits of memristor programming. This soft threshold is more consistent with biology than a hard threshold device in that biological spike-frequency adaptation is governed by ionic concentrations changing populations of conductances [69].

In order to mimic spike-frequency adaptation, there are two reasons this circuit must use a volatile memristor. First, after the circuit has been stimulated by an input above the high voltage programming threshold such that the memristor becomes programmed, it is necessary for the circuit to recover back to the un-programmed state. While it may be possible to accomplish this with a non-volatile memristor and some extra

circuitry, a volatile memristor can be implemented in a single device without additional wiring and will improve the overall circuit density. Second, the ability of the circuit to produce repeatable pulses for a range of small value inputs and then adapt for larger inputs cannot be achieved with a non-volatile memristor.

As shown in Figure 18, as D approaches zero and the memristor becomes non-volatile the range of stable input voltages where the memristor does not program collapses to a single value. This collapse occurs because without the restoring feedback, non-volatile memristors cannot balance the programming voltages from the pulses and inter-pulse intervals.

CHAPTER 6

CONCLUTIONS AND FUTURE WORK

6.1 *Summary and Contributions*

With the ITRS's prediction of an impending end to Moore's Law in CMOS digital computing and the already observed saturation in chip performance, neuromorphic computing is one of a few novel computing architectures that may advance application specific performance for the future. By replicating the architecture of the biological brain, low power adaptive systems should be possible that excel at pattern recognition, control, and processing noisy data. Mixed ion-electron conducting memristors have become an increasingly important component within neuromorphic circuitry.

This work first derived a physics based model for mixed ion-electron conducting memristors based on the activated hopping conductivity of ions within the device. It was shown that the full exponential form of hopping conductivity is necessary at high electric fields, but can be simplified to a linear drift-diffusion model at low electric fields. Using this physical model it was shown that experimentally observed ion profiles are modelled as the device size and electric field is changed resulting in an abrupt transition in small devices with high electric fields or a smooth gradient in large devices with low electric fields.

While the derived physical model may be useful for complex finite element models, it is too computationally intensive for large scale circuit simulations. Therefore, a simplified model based on the original memristor definition, but retaining the activated ion hopping conductivity from the physical model, was developed for use in simple

circuit model elements. This generalized mixed ion-electron conducting memristor model was verified in two extreme examples. The first example was a well-studied nanoscale non-volatile filamentary memristor exhibiting binary switching at elevated temperatures and memory retention over many years. The second example was a less well-studied macroscale volatile memristor that exhibits a continuous range of resistance states and ionic diffusion at room temperature.

Lastly, the volatile memristor model was added to a Schmitt Trigger circuit in order to add volatile functionality relevant to neuromorphic computing by implementing the thresholding and spike generation components of a neuromorphic circuit. It was shown that by including a volatile memristor the circuit exhibits spike-frequency adaptation, a biological mechanism important in the prevention of seizures.

6.2 *Future Work*

Two aspects of this work could be expanded. First, the two example devices modeled in this work relied on assumptions to keep the model computationally simple. For the nanoscale non-volatile filamentary memristor, a mobility scaling factor was used to compensate for the nonlinear high field mobility and a uniform effective ion concentration was assumed. While these assumptions reproduced experimentally observed features, a more precise model may be achievable at the cost of computational simplicity. For the macroscale volatile memristor, a low frequency cubic ion gradient was assumed. This assumption is valid for the low frequencies encountered in biological systems, but more complex behavior, such a double layer capacitance, is encountered at high frequencies. These features may be useful as dynamic filters.

Likewise, it was shown that the linear steady state ion distribution shown in previous work is incompatible with the current continuity equations for the simplifying assumptions made in this model, particularly the assumption of quasi-electroneutrality. Future work may explore relaxing these assumptions and adding features such as a dynamic space charge.

The second opportunity to expand this work is in the number of circuits relevant to neuromorphic computing that were not modelled. Such circuits include amplifiers, filters, and neuristor circuits that may exhibit biologically relevant behavior when a volatile memristor is included.

REFERENCES

[1] (2013). *International Technology Roadmap for Semiconductors*. Available: www.itrs.net

[2] I. L. Markov, "Limits on fundamental limits to computation," *Nature,* vol. 512, pp. 147-154, 2014.

[3] S. E. Thompson and S. Parthasarathy, "Moore's law: the future of Si microelectronics," *Materials Today,* vol. 9, pp. 20-25, 2006.

[4] J. Wang and M. Lundstrom, "Does source-to-drain tunneling limit the ultimate scaling of MOSFETs?," in *Electron Devices Meeting, 2002. IEDM'02. International*, 2002, pp. 707-710.

[5] V. V. Zhirnov, R. K. Cavin, J. A. Hutchby, and G. I. Bourianoff, "Limits to binary logic switch scaling-a gedanken model," *Proceedings of the IEEE,* vol. 91, pp. 1934-1939, 2003.

[6] J. Hruska. (2014). *Stop obsessing over transistor counts: It's a terrible way of comparing chips*. Available: http://www.extremetech.com/computing/190946-stop-obsessing-over-transistor-counts-theyre-a-terrible-way-of-comparing-chips

[7] C. Mead, "Neuromorphic electronic systems," *Proceedings of the IEEE,* vol. 78, pp. 1629-1636, 1990.

[8] J. Georgiou, E. M. Drakakis, C. Toumazou, and P. Premanoj, "An analogue micropower log-domain silicon circuit for the Hodgkin and Huxley nerve axon," in *Circuits and Systems, 1999. ISCAS'99. Proceedings of the 1999 IEEE International Symposium on*, 1999, pp. 286-289.

[9] F. Folowosele, A. Harrison, A. Cassidy, A. G. Andreou, R. Etienne-Cummings, S. Mihalas, E. Niebur, and T. J. Hamilton, "A switched capacitor implementation of the generalized linear integrate-and-fire neuron," in *Circuits and Systems, 2009. ISCAS 2009. IEEE International Symposium on*, 2009, pp. 2149-2152.

[10] D. B. Strukov, G. S. Snider, D. R. Stewart, and R. S. Williams, "The missing memristor found," *Nature,* vol. 453, pp. 80-83, 2008.

[11] A. Thomas, "Memristor-based neural networks," *Journal of Physics D: Applied Physics,* vol. 46, p. 093001, 2013.

[12] E. Gale, B. D. L. Costello, and A. Adamatzky, "Observation and characterization of memristor current spikes and their application to neuromorphic computation," in *NUMERICAL ANALYSIS AND APPLIED MATHEMATICS ICNAAM 2012: International Conference of Numerical Analysis and Applied Mathematics*, 2012, pp. 1898-1901.

[13] Y. V. Pershin and M. Di Ventra, "Experimental demonstration of associative memory with memristive neural networks," *Neural Networks,* vol. 23, pp. 881-886, 2010.

[14] B. Linares-Barranco and T. Serrano-Gotarredona, "Exploiting memristance in adaptive asynchronous spiking neuromorphic nanotechnology systems," in *Nanotechnology, 2009. IEEE-NANO 2009. 9th IEEE Conference on*, 2009, pp. 601-604.

[15] B. Linares-Barranco, T. Serrano-Gotarredona, L. A. Camuñas-Mesa, J. A. Perez-Carrasco, C. Zamarreño-Ramos, and T. Masquelier, "On Spike-Timing-

Dependent-Plasticity, Memristive Devices, and building a Self-Learning Visual Cortex," *Frontiers in Neuroscience,* vol. 5, 2011-March-17 2011.
[16] G. Fuhrmann, H. Markram, and M. Tsodyks, "Spike frequency adaptation and neocortical rhythms," *Journal of Neurophysiology,* vol. 88, pp. 761-770, 2002.
[17] J. Benda, A. Longtin, and L. Maler, "Spike-frequency adaptation separates transient communication signals from background oscillations," *The Journal of neuroscience,* vol. 25, pp. 2312-2321, 2005.
[18] S. Verma-Ahuja, M. Steven Evans, and T. L. Pencek, "Evidence for decreased calcium dependent potassium conductance in hippocampal CA3 neurons of genetically epilepsy-prone rats," *Epilepsy research,* vol. 22, pp. 137-144, 1995.
[19] L. O. Chua, "Memristor-The missing circuit element," *Circuit Theory, IEEE Transactions on,* vol. 18, pp. 507-519, 1971.
[20] L. O. Chua and K. Sung Mo, "Memristive devices and systems," *Proceedings of the IEEE,* vol. 64, pp. 209-223, 1976.
[21] M. A. C. Maher, S. P. Deweerth, M. A. Mahowald, and C. A. Mead, "Implementing neural architectures using analog VLSI circuits," *Circuits and Systems, IEEE Transactions on,* vol. 36, pp. 643-652, 1989.
[22] G. Indiveri, B. Linares-Barranco, T. J. Hamilton, A. van Schaik, R. Etienne-Cummings, T. Delbruck, S.-C. Liu, P. Dudek, P. Häfliger, S. Renaud, J. Schemmel, G. Cauwenberghs, J. Arthur, K. Hynna, F. Folowosele, S. SAÏGHI, T. Serrano-Gotarredona, J. Wijekoon, Y. Wang, and K. Boahen, "Neuromorphic silicon neuron circuits," *Frontiers in Neuroscience,* vol. 5, 2011-May-31 2011.
[23] E. H. Chudler. *Brain Facts and Figures*. Available: http://faculty.washington.edu/chudler/facts.html
[24] W. Gerstner, A. K. Kreiter, H. Markram, and A. V. Herz, "Neural codes: firing rates and beyond," *Proceedings of the National Academy of Sciences,* vol. 94, pp. 12740-12741, 1997.
[25] G. L. Fain, *Molecular and Cellular Physiology of Neurons*. Cambridge, Mass: Harvard University Press, 1999.
[26] A. L. Hodgkin and A. F. Huxley, "A quantitative description of membrane current and its application to conduction and excitation in nerve," *The Journal of physiology,* vol. 117, pp. 500-544, 1952.
[27] M. D. Pickett, G. Medeiros-Ribeiro, and R. S. Williams, "A scalable neuristor built with Mott memristors," *Nat Mater,* vol. 12, pp. 114-117, 2013.
[28] H. Markram, W. Gerstner, and P. J. Sjöström, "A history of spike-timing-dependent plasticity," *Frontiers in synaptic neuroscience,* vol. 3, 2011.
[29] T. Prodromakis, C. Toumazou, and L. Chua, "Two centuries of memristors," *Nature materials,* vol. 11, p. 478, 2012.
[30] S. D. Ha and S. Ramanathan, "Adaptive oxide electronics: A review," *Journal of Applied Physics,* vol. 110, p. 071101, 2011.
[31] R. Waser and M. Aono, "Nanoionics-based resistive switching memories," *Nature materials,* vol. 6, pp. 833-840, 2007.
[32] M. J. Lee, S. I. Kim, C. B. Lee, H. Yin, S. E. Ahn, B. S. Kang, K. H. Kim, J. C. Park, C. J. Kim, and I. Song, "Low-Temperature-Grown Transition Metal Oxide Based Storage Materials and Oxide Transistors for High-Density Non-volatile Memory," *Advanced Functional Materials,* vol. 19, pp. 1587-1593, 2009.

[33] X. Liu, S. M. Sadaf, S. Kim, K. P. Biju, X. Cao, M. Son, S. H. Choudhury, G.-Y. Jung, and H. Hwang, "Improvement of Resistive Switching Uniformity by Introducing a Thin NbOx Interface Layer," *ECS Solid State Letters,* vol. 1, pp. Q35-Q38, 2012.
[34] J. J. Yang, M. Zhang, J. P. Strachan, F. Miao, M. D. Pickett, R. D. Kelley, G. Medeiros-Ribeiro, and R. S. Williams, "High switching endurance in TaOx memristive devices," *Applied Physics Letters,* vol. 97, p. 232102, 2010.
[35] H. Sim, D. Choi, D. Lee, S. Seo, M.-J. Lee, I.-K. Yoo, and H. Hwang, "Resistance-switching characteristics of polycrystalline Nb 2 O 5 for nonvolatile memory application," *Electron Device Letters, IEEE,* vol. 26, pp. 292-294, 2005.
[36] T.-W. Lee and J. H. Nickel, "Memristor resistance modulation for analog applications," *Electron Device Letters, IEEE,* vol. 33, pp. 1456-1458, 2012.
[37] D.-H. Kwon, K. M. Kim, J. H. Jang, J. M. Jeon, M. H. Lee, G. H. Kim, X.-S. Li, G.-S. Park, B. Lee, and S. Han, "Atomic structure of conducting nanofilaments in TiO2 resistive switching memory," *Nature nanotechnology,* vol. 5, pp. 148-153, 2010.
[38] R. Münstermann, J. J. Yang, J. P. Strachan, G. Medeiros-Ribeiro, R. Dittmann, and R. Waser, "Morphological and electrical changes in TiO2 memristive devices induced by electroforming and switching," *physica status solidi (RRL)-Rapid Research Letters,* vol. 4, pp. 16-18, 2010.
[39] J. P. Strachan, D. B. Strukov, J. Borghetti, J. J. Yang, G. Medeiros-Ribeiro, and R. S. Williams, "The switching location of a bipolar memristor: chemical, thermal and structural mapping," *Nanotechnology,* vol. 22, p. 254015, 2011.
[40] M. Noman, A. A. Sharma, Y. M. Lu, R. Kamaladasa, M. Skowronski, P. A. Salvador, and J. A. Bain, "Mechanism of localized electrical conduction at the onset of electroforming in TiO2 based resistive switching devices," *Applied Physics Letters,* vol. 104, p. 113510, 2014.
[41] S. H. Jo, T. Chang, I. Ebong, B. B. Bhadviya, P. Mazumder, and W. Lu, "Nanoscale Memristor Device as Synapse in Neuromorphic Systems," *Nano Letters,* vol. 10, pp. 1297-1301, 2010/04/14 2010.
[42] J. D. Greenlee, W. Calley, W. Henderson, and W. A. Doolittle, "Halide based MBE of crystalline metals and oxides," *Physica status solidi (c),* vol. 9, pp. 155-160, 2012.
[43] J. D. Greenlee, J. C. Shank, M. B. Tellekamp, B. Gunning, C. A. Fabien, and A. Doolittle, "Liquid Phase Electro-Epitaxy of Memristive $LiNbO_2$ Crystals," *Crystal Growth & Design,* vol. 14, pp. 2218-2222, 2014.
[44] V. Erokhin, T. Berzina, and M. P. Fontana, "Hybrid electronic device based on polyaniline-polyethyleneoxide junction," *Journal of Applied Physics,* vol. 97, p. 064501, 2005.
[45] J. D. Greenlee, C. F. Petersburg, W. G. Daly, F. M. Alamgir, and W. A. Doolittle, "In situ investigation of the channel conductance of a $Li_{1-x}CoO_2$ ($0< x< 0.5$) ionic-electronic transistor," *Applied Physics Letters,* vol. 102, p. 213502, 2013.
[46] Y. V. Pershin and M. Di Ventra, "Spin memristive systems: Spin memory effects in semiconductor spintronics," *Physical Review B,* vol. 78, p. 113309, 2008.

[47] X. Wang, Y. Chen, H. Xi, H. Li, and D. Dimitrov, "Spintronic memristor through spin-torque-induced magnetization motion," *Electron Device Letters, IEEE,* vol. 30, pp. 294-297, 2009.
[48] H. Mahmoudi, T. Windbacher, V. Sverdlov, and S. Selberherr, "Implication logic gates using spin-transfer-torque-operated magnetic tunnel junctions for intrinsic logic-in-memory," *Solid-State Electronics,* vol. 84, pp. 191-197, 2013.
[49] A. Chanthbouala, V. Garcia, R. O. Cherifi, K. Bouzehouane, S. Fusil, X. Moya, S. Xavier, H. Yamada, C. Deranlot, and N. D. Mathur, "A ferroelectric memristor," *Nature materials,* vol. 11, pp. 860-864, 2012.
[50] D. B. Strukov, J. L. Borghetti, and R. S. Williams, "Coupled Ionic and Electronic Transport Model of Thin-Film Semiconductor Memristive Behavior," *small,* vol. 5, pp. 1058-1063, 2009.
[51] P. R. Mickel, A. J. Lohn, B. J. Choi, J. J. Yang, M.-X. Zhang, M. J. Marinella, C. D. James, and R. S. Williams, "A physical model of switching dynamics in tantalum oxide memristive devices," *Applied Physics Letters,* vol. 102, p. 223502, 2013.
[52] J. D. Greenlee, J. C. Shank, M. B. Tellekamp, and W. A. Doolittle, "Spatiotemporal drift-diffusion simulations of analog ionic memristors," *Journal of Applied Physics,* vol. 114, p. 034504, 2013.
[53] Z. Biolek, D. Biolek, and V. Biolková, "SPICE model of memristor with nonlinear dopant drift," *Radioengineering,* vol. 18, pp. 210-214, 2009.
[54] P. R. Mickel, A. J. Lohn, and M. J. Marinella, "Detection and characterization of multi-filament evolution during resistive switching," *Applied Physics Letters,* vol. 105, p. 053503, 2014.
[55] H. Abdalla and M. D. Pickett, "SPICE modeling of memristors," in *Circuits and Systems (ISCAS), 2011 IEEE International Symposium on*, 2011, pp. 1832-1835.
[56] N. Mott, "Conduction in glasses containing transition metal ions," *Journal of Non-Crystalline Solids,* vol. 1, pp. 1-17, 1968.
[57] A. Nenashev, F. Jansson, S. Baranovskii, R. Österbacka, A. Dvurechenskii, and F. Gebhard, "Hopping conduction in strong electric fields: Negative differential conductivity," *Physical Review B,* vol. 78, p. 165207, 2008.
[58] J. D. Greenlee, W. Calley, M. W. Moseley, and W. A. Doolittle, "Comparison of Interfacial and Bulk Ionic Motion in Analog Memristors," *IEEE Transactions on Electron Devices,* vol. 60, pp. 427-432, 2013.
[59] J. D. Greenlee, C. F. Petersburg, W. Laws Calley, C. Jaye, D. A. Fischer, F. M. Alamgir, and W. Alan Doolittle, "In-situ oxygen x-ray absorption spectroscopy investigation of the resistance modulation mechanism in $LiNbO_2$ memristors," *Applied Physics Letters,* vol. 100, pp. 182106-182106-4, 2012.
[60] A. Leshem, E. Gonen, and I. Riess, "Nonlinear I–V relations and hysteresis in solid state devices based on oxide mixed-ionic–electronic conductors," *Nanotechnology,* vol. 22, p. 254024, 2011.
[61] I. Riess and J. Maier, "Symmetrized General Hopping Current Equation," *Physical review letters,* vol. 100, p. 205901, 2008.
[62] Y. Nian, J. Strozier, N. Wu, X. Chen, and A. Ignatiev, "Evidence for an oxygen diffusion model for the electric pulse induced resistance change effect in transition-metal oxides," *Physical review letters,* vol. 98, p. 146403, 2007.

[63] M. J. Geselbracht, A. M. Stacy, A. R. Garcia, B. G. Silbernagel, and G. H. Kwei, "Local environment and lithium ion mobility in lithium niobate ($LiNbO_2$): inferences from structure, physical properties, and NMR," *The Journal of Physical Chemistry,* vol. 97, pp. 7102-7107, 1993.

[64] A. McDowell, D. Snyderman, M. S. Conradi, B. Silbernagel, and A. Stacy, "Cross relaxation and atomic motion in $LiNbO_2$," *Physical Review B,* vol. 50, p. 15764, 1994.

[65] P. Kofstad, P. Anderson, and O. Krudtaa, "Oxidation of titanium in the temperature range 800–1200 C," *Journal of the Less Common Metals,* vol. 3, pp. 89-97, 1961.

[66] C. Bean, J. Fisher, and D. Vermilyea, "Ionic conductivity of tantalum oxide at very high fields," *Physical Review,* vol. 101, p. 551, 1956.

[67] J. J. Yang, M. D. Pickett, X. Li, D. A. Ohlberg, D. R. Stewart, and R. S. Williams, "Memristive switching mechanism for metal/oxide/metal nanodevices," *Nature nanotechnology,* vol. 3, pp. 429-433, 2008.

[68] Y. V. Pershin and M. Di Ventra, "Practical Approach to Programmable Analog Circuits With Memristors," *Circuits and Systems I: Regular Papers, IEEE Transactions on,* vol. 57, pp. 1857-1864, 2010.

[69] B. W. Connors, M. J. Gutnick, and D. A. Prince, "Electrophysiological properties of neocortical neurons in vitro," *Journal of Neurophysiology,* vol. 48, pp. 1302-1320, December 1, 1982 1982.